The Morphology of Slow-Slipping Oceanic Transform Faults on the Mid-Atlantic Ridge

Emma Woodford

A thesis

submitted to the faculty of

the Department of Earth and Environmental Sciences

in partial fulfillment

of the requirements for the degree of

Master of Science

Boston College
Morrissey College of Arts and Sciences
Graduate School

2024

The Morphology of Slow-Slipping Oceanic Transform Faults on the Mid-Atlantic Ridge
Emma Woodford

Advisor: Mark D. Behn

The global mid ocean ridge system is segmented by transform faults and non-transform discontinuities. Oceanic transform faults display distinct morphology characterized by a deep valley and shallow transverse ridges on either side of the valley. Although the morphology of oceanic transform faults is known to first order, there is no consensus on the processes that form the transform valley and/or the adjacent transverse ridges. To date, most models of transform morphology attribute these features to either transform-normal extension or to shear stresses induced by slip along the fault. In this thesis, I compile bathymetric data along 16 major transform faults on the Mid-Atlantic Ridge and identify the key morphological properties of each transform. Specifically, I estimate transform valley width, depth, and total relief measured from the valley floor to the adjacent transverse ridges. The strongest correlation is between the relief and maximum depth, but there is a weaker correlation between maximum depth and valley width. These morphologic properties are then compared to key fault parameters such as slip rate, fault-normal compression/extension rate, thermal area, and the seismic coupling ratio, which is defined as the fraction of total fault slip that occurs seismically. These comparisons are used to test models that describe mechanisms of the formation of the transform valley. The strongest correlation is between the fault thermal area and valley half width. This suggests that the width of the transform valley may be controlled by the shear stress applied to the fault as it slips. By contrast, the data are not

consistent with a model in which the valley is created by extension across the fault, because our data show that the maximum transform valley depth increases with compression and not extension.

Table of Contents

Acknowledgements

I would like to firstly thank my advisor Dr. Mark Behn for his guidance and support throughout my master's career. I also appreciate all of the ideas and insight from my weekly meetings with Dr. Thomas Morrow, Dr. Xiaochuan Tian, Dr. Garrett Apuzen-Ito and Dr. Jana Schierjott. This research was supported by the NSF through the OCE-19-28776 award. Finally, I would like to thank Dr. Noah Snyder for reviewing and helping with this thesis.

LIST OF TABLES

LIST OF FIGURES

1. Introduction

The Earth's lithosphere is made up of rigid tectonic plates that move relative to one another over the underlying, low viscosity asthenosphere. Mid-ocean ridges (MORs) are locations where two tectonic plates diverge and the asthenosphere upwells to fill the newly created gap, undergoing decompression melting to form the oceanic crust. As the plates drift away from the ridge axis, the new lithosphere cools and contracts, and its average density increases. As this happens the lithosphere subsides to maintain isostatic equilibrium, giving the ocean basins their characteristic age-deepening bathymetric expression. This global pattern of subsidence away from mid-ocean ridges has been explained using a half-space cooling model, in which the mantle cools over time by thermal conduction from the surface (e.g., Parsons & Sclater, 1977; Stein & Stein, 1992).

In addition to the temperature-dependence of rock density, the strength of crust and mantle rocks is also dependent on temperature, with rock strength increasing with decreasing temperature. Thus, another implication of the half-space cooling model is that the lithosphere should thicken and strengthen with distance from the ridge axis. One expression of this strengthening is the correlation of the maximum depth of intra-plate earthquakes with the 600ºC isotherm predicted from the half-space cooling model (e.g., Craig et al., 2014). The strengthening of the plate with age is also expressed as an increase in effective elastic thickness, which describes how the lithosphere flexes under a topographic load, such as a seamount (Watts et al., 1980). Calculations show that the effective elastic thickness increases with the age of the lithosphere, with thicknesses ranging from a few kilometers at the ridge axis to about 30 km at ages of at least 80 Ma, consistent with the predictions of the half-space cooling model (Watts et al., 1980).

1.2 Mid ocean ridges

While the half-space cooling model provides a first-order explanation for global-scale patterns of seafloor bathymetry and lithospheric strength that are independent of spreading rate, the near-axis morphology of slow and fast spreading mid-ocean ridges is significantly more variable (Figure 1). Slow spreading ridges (such as the Mid-Atlantic Ridge) are characterized by an axial ridge valley (Figure 1b). These ridge valleys can be tens of kilometers wide and two to three kilometers deep with faulted sides (e.g., Macdonald et al., 1982; Sempéré et al., 1993). The valley walls are formed by inward-dipping normal faults with vertical displacements of several hundred meters (Heezen, 1960). The valley floor consists of a neovolcanic zone, where new crust is formed through volcanic activity. Gravity anomalies show that the across-axis morphology of typically slow spreading ridges is not isostatically compensated, indicating that the observed morphology cannot be explained solely by crustal thickness variations (Phipps Morgan et al., 1987; Neumann & Forsyth, 1993). This implies that the ridge valley relief must be at least partially supported by the internal strength of axial lithosphere (Lin & Parmentier, 1989).

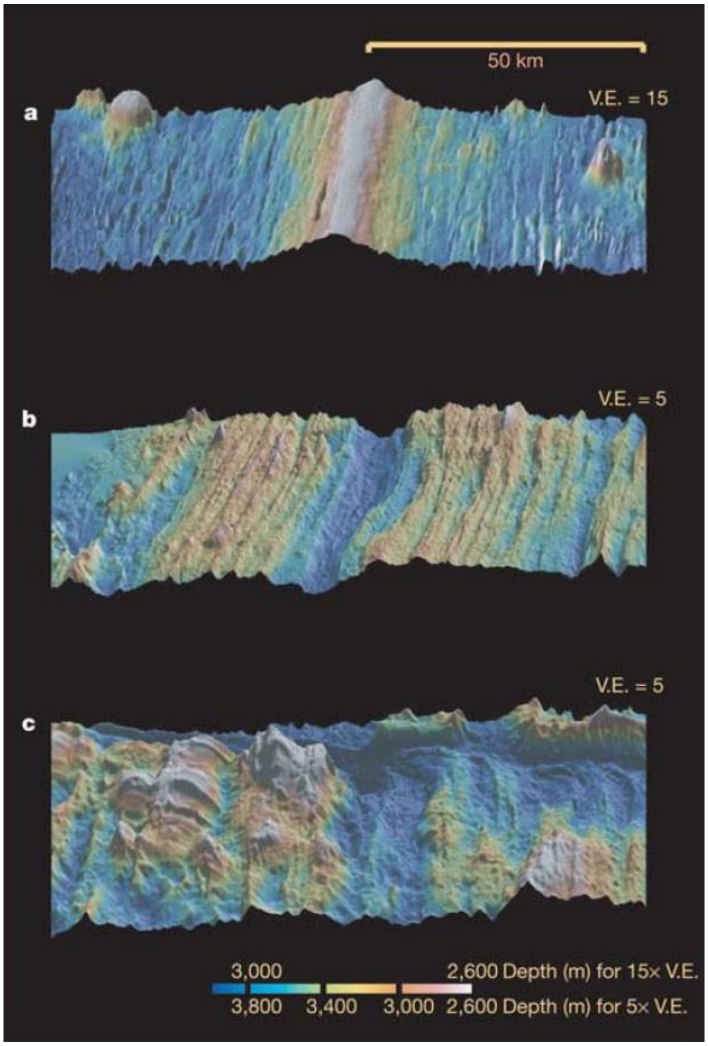

Figure 1: Bathymetry in 40-km wide swaths across a (a) fast and (b) slow spreading center. Panel (c) shows the intersection of a slow spreading center with an adjacent transform fault. Note that the seafloor is deeper along the active transform fault and in the corresponding fracture zones compared to the adjacent seafloor. Figure from Buck et al. (2005).

Seafloor spreading at slow-spreading ridges is accommodated by a combination of dike intrusion in the neovolcanic zone and tectonic faulting that forms the ridge valley walls (Searle, 2013). In 2-D models of faulting and magma intrusion at a spreading ridge, the ridge valley morphology that develops is dependent on the amount of magma intrusion relative to the amount of tectonic stretching (Buck et al., 2005; Behn & Ito, 2008; Olive et al., 2015). As the rate of magma intrusion decreases relative to the total amount of far-field extension, larger and more widely spaced normal faults develop; with large-offset detachment faults (Figure 1c) forming when approximately half the total plate separation is accommodated by magma intrusion (Buck et al., 2005; Tucholke et al., 2008). These normal faults create the axial morphology observed in typical slow spreading ridge environments. Over multiple fault cycles, these models show that faulting follows a pattern of initiation, growth, and termination, with each new fault initiating on the opposite side of the ridge axis (Buck et al., 2005; Behn & Ito, 2008). An active normal fault will initiate near the ridge axis and will begin to move away from the ridge axis due to magmatic accretion. As the fault moves away, another fault will form on the opposite side of the axis in the location of the highest tensile stresses (Schierjott et al., 2023). This pattern of alternating faulting is thought to be the mechanism that creates the axial valley present at slow spreading ridges (Behn & Ito, 2008), with the depth and width of the ridge valley related to the rate of magmatic intrusion and the axial lithospheric thickness.

In contrast to slow-spreading mid-ocean ridges, fast-spreading ridges, such as the East Pacific Rise, do not have a ridge valley. Instead, their flanks rise towards the ridge axis, forming a small axial high that is 100–500 m tall and a few kilometers wide (Figure 1a). Similar to slow spreading ridges, the axis of a fast-spreading ridge is characterized by a neovolcanic zone where small normal faults and fissures form (Macdonald, 1982). In some cases, fast spreading ridges are characterized by a shield volcano-like shape with a summit ridge. Overall, the first-order character of axial high morphology at fast spreading ridges is thought to reflect a combination of hotter, thinner lithosphere and greater amounts of magma intrusion as compared to slow-spreading ridges (Shaw & Lin, 1996; Buck et al., 2005).

These differences in axial morphology as a function of spreading rate also correspond to differences in the gravity signature of mid-ocean ridges (Searle, 2013). While ridges spreading slower than ~60 mm/yr typically have large amplitude negative gravity anomalies indicating that the ridge axis is out of isostatic equilibrium, ridges spreading faster than 70 mm/yr typically have only small gravity anomalies suggesting the axial high is fully compensated (Talwani et al., 1971). This observation is consistent with thinner, weaker lithosphere at faster spreading ridges that does not support significant topographic relief.

1.2 Transform faults

Mid-ocean ridges are separated into individual spreading segments 10s to 100s of kilometers long by transform and non-transform offsets (Macdonald et al., 1988; Sempéré et al, 1993). Offsets on mid-ocean ridges are classified based on their morphology, length, and spatial stability over time and are often described as different order discontinuities (Sempéré et al, 1993). Transform faults represent the first-order segmentation of mid-ocean ridges, ranging from ~30 to 1000 km in length. Transform faults accommodate the relative strike-slip motion between two plates and trace small circles on the sphere centered around an Euler rotation axis (Wilson, 1965). Earthquakes on transform faults display focal mechanisms consistent with strike slip motion, while earthquakes located on the crest of the ridge axis show predominantly normal faulting motion (Sykes 1967).

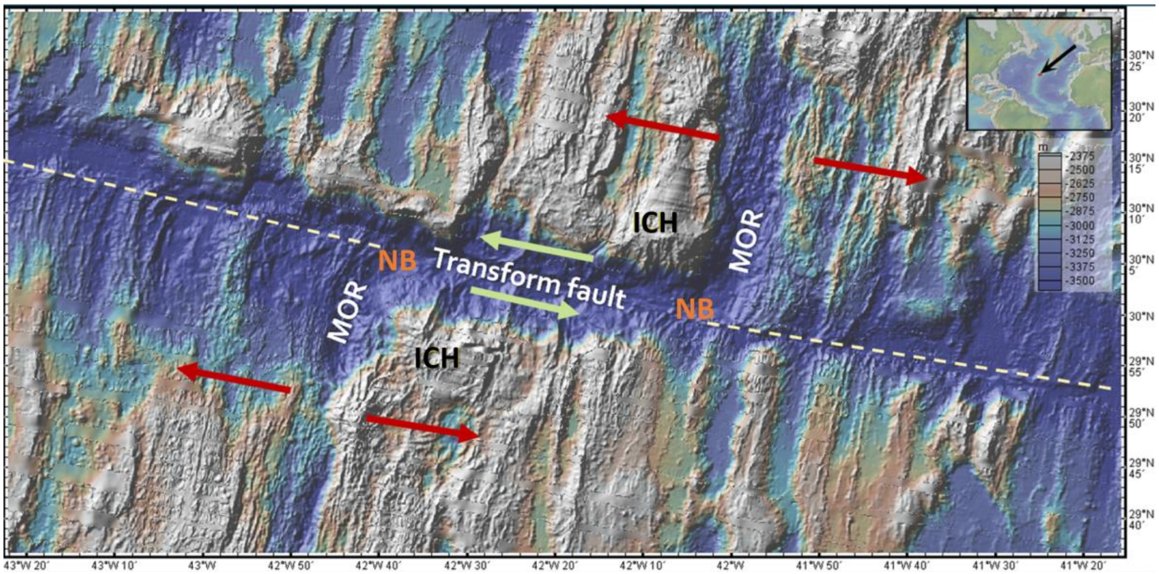

Figure 2: Bathymetry of the Atlantis Transform Fault at 30ºN on the slow spreading Mid-Atlantic Ridge. Dark blue bathymetry represents deeper sections of the fault; lighter colors represent shallow sections of the fault. The fracture zones, which trace the inactive fracture zone off-axis, are highlighted with dashed lines; inside corner highs (ICH) associated with large-offset detachment faults are indicated.

Transform faults are often characterized by a valley that runs parallel to the fault. Transform valleys display similarities to axial ridge valleys, with depth anomalies of 1000–2500 m relative to the surrounding seafloor and elevated shoulders (Figure 2). Transform faults also leave traces (termed fracture zones) in the off-axis seafloor that are colinear to the active fault. Fracture zones retain the age offset of the seafloor generated by the original transform fault; however, fracture zones do not accommodate active fault slip (Morrow et al. 2019). Some transform faults, like the Kane transform on the Mid-Atlantic Ridge, have fracture zones that can be traced all the way back to the continental margin (Tucholke & Schouten, 1988). Recent observations show that transform valleys are systematically deeper than their adjacent fracture zones

(Grevemeyer et al., 2021), suggesting a complex pattern of accretion and tectonic reorganization near ridge-transform intersections.

At slow spreading ridges, transform fault valleys can be divided into two morphotectonic groups (Karson et al., 1983). The first group consists of transform valleys that are less than 4-km wide and are centered on a zone of tectonism that is characterized by irregular topography associated with recent faulting. The second group is composed of wider valleys (10s of km in width) with steep symmetric walls on either side of the zone of tectonism. The Atlantis transform fault (Figure 2) as well as all of the transform faults in this study are from the second group. The slopes of the valley walls are controlled by sediment deposition and mass wasting processes (Karson and Dick, 1983).

Transform valleys often deepen near ridge transform intersections, producing deep nodal basins (NB) (Figure 2). It has been hypothesized that these nodal basins result from viscous head loss in the asthenosphere combined with the opposing old colder lithosphere (Sleep and Biehler, 1970). Slow slipping transform faults also display asymmetric morphology near their intersection with a spreading segment. The “inside corner”, located between the ridge axis and active transform fault (Figure 2), is typically shallower compared to conjugate “outside corner”, where the lithosphere is more strongly coupled to the older lithosphere across the fracture zone. Many inside corners are sites of oceanic core complexes that form through detachment normal faulting (Cann et al., 1997; Schierjott et al., 2023).

Similar to mid-ocean ridges, the morphology of transform faults varies with spreading rate. Faster slipping transforms typically have shallower valleys than slower slipping transform faults (Parmentier and Phipps Morgan, 1990). Further, transform faults at a fast-spreading ridges are often segmented into several smaller transform faults with small ridge-like sections (or intra-transform spreading centers) between them. Finally, the deep nodal basins that are present at slow spreading centers, are typically not seen at transform faults at fast spreading centers (Luo et al., 2021).

Higher order segmentation of mid-ocean ridges describes progressively smaller and less stable offsets, often known as non-transform offsets (Macdonald et al., 1988). Non-transform offsets are different than transform faults because they are not defined by a single fault trace, but instead consist of a complex zone of trans-tensional faulting. Non-transform offsets are typically shorter in length and have a more diffuse morphology compared to transform faults (Searle, 2013). Second order non-transform offsets often exist between spreading segments that have different tectonic styles, levels of magmatic activity, and extensional rates (Karson, 1990). Second order offsets can have off-axis discordant zones that are not parallel to plate motion and display fault geometries characterized by oblique slip. Third order offsets are similar to second order offsets; however, they do not have recognizable off axis traces, implying they are short lived or are newly formed second order offsets (Sempéré et al, 1993). Finally, fourth order segmentation represents minor offsets along a spreading center that extend for less than 4 km and usually exist solely within the neo-volcanic zone of the ridge axis. The small size of fourth-order offsets is often entirely contained within the axial ridge valley

(Sempéré et al, 1993). A common example of a fourth order offset is two overlapping ridge segments separated by an elongate depression (Sempéré et al, 1993).

The cause of mid-ocean ridge segmentation remains a topic of debate. Models that have been proposed include inheritance from continental margins (Pockalny et.al, 1997) and three-dimensional (3-D) patterns of mantle upwelling along the ridge (e.g., Lin et al., 1990; Sempéré et al., 1993). In the later model, the wavelength of segmentation is controlled by the 3-D pattern of mantle upwelling, with ridge segments centered over regions of upwelling and decompression melting and offsets formed between locations of strong upwelling (Schouten et al., 1985; Parmentier and Phipps Morgan, 1990; Choblet & Parmentier, 2001). Spreading segment centers are typically shallower than segment ends, and the undulation of the depth from segment center to segment ends is thought to be caused by variations in crustal thickness associated with more melting at centers of upwelling and less melting toward offsets (Lin et al., 1990; Tolstoy et al., 1993). Flexural compensation associated with these variations in crustal thickness have been speculated to contribute to the formation of transform valleys (Chen & Lin, 1999).

1.3 Motivation

While the origin of mid-ocean ridge morphology and its sensitivity to spreading rate has been studied in detail (e.g., Buck et al., 2005; Tucholke et al., 2008; Behn & Ito, 2008), the origin of transform valley morphology has received significantly less attention and remains poorly understood. To date there has been no systematic study comparing transform morphology to ridge morphology across different spreading environments, and there remains no consensus on the physical processes by which transform valleys form.

As described above, bathymetric data has played a key role in distinguishing different models for the formation of the axial ridge valley. However, comparable comprehensive datasets of transform fault morphology have not been compiled, nor have the few existing models for transform valley formation been systematically compared to bathymetric data from natural transform faults. This thesis will thus represent a first step at creating such a database by systematically characterizing the morphology of a series of oceanic transform faults along the slow-spreading Mid-Atlantic Ridge. To characterize transform morphology, I quantify different morphologic parameters of transform valleys, including their width, depth, and relief. For comparison, I evaluate the same morphologic parameters for the adjacent axial ridge valleys. This dataset is then used to evaluate different models for the formation of transform valleys that have been proposed in the literature.

2. Methods

In this thesis, I analyzed the bathymetry of 11 oceanic transform faults along the slow-spreading Mid-Atlantic Ridge (Figure 3). I chose the Mid-Atlantic Ridge due to the availability of high-quality bathymetric data and because it has many examples of classic transform fault morphology with well-defined transform valleys. Here I use the Oceanographer transform fault located at 35ºN on the northern Mid-Atlantic Ridge, and one of the 11 transform faults I investigated, to demonstrate the methods I used throughout my analysis. After illustrating my approach for the Oceanographer transform fault, I show results from all the transform faults I analyzed and compare them with different external parameters that may influence transform fault morphology.

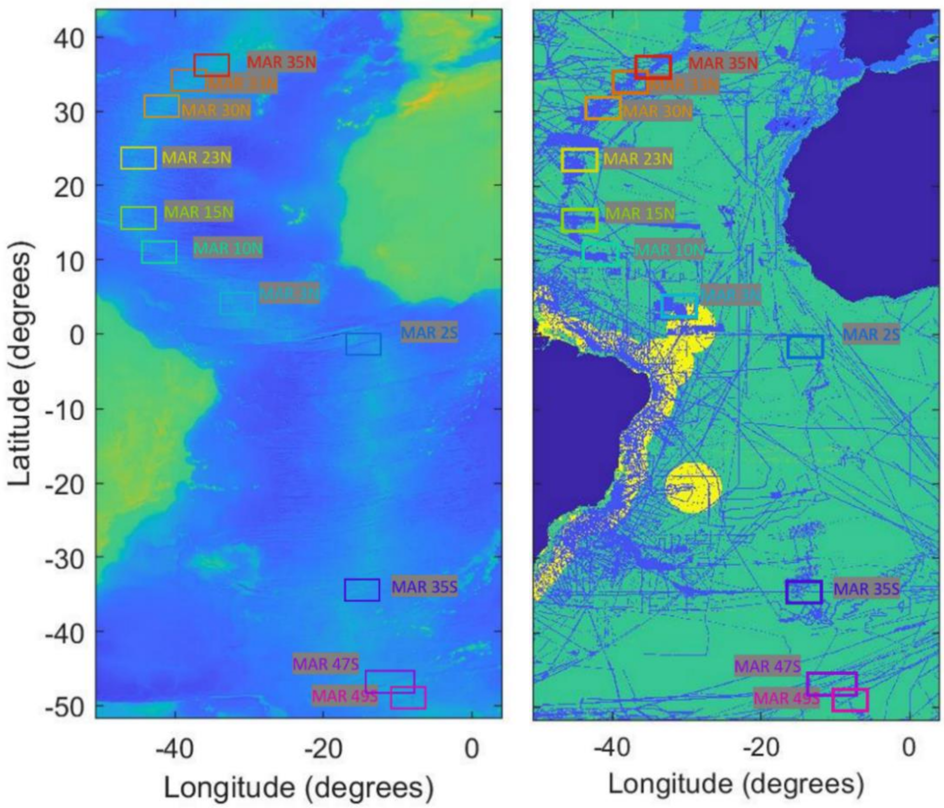

Figure 3: (left) Bathymetry of the Atlantic Ocean downloaded from GEBCO_2021. Boxes denote location of transform faults analyzed in this study. The colors of the boxes correlate with each individual transform faults (right) Data sources used to infer bathymetry. Blue lines represent direct measurements, green spaces represent satellite-derived data, yellow spaces represent mixed source data types (e.g., combination of single beam, multibeam, interpolation).

2.1 Bathymetric data

The bathymetry data used in this study comes from the GEBCO_2021 dataset (GEBCO Compilation Group, 2021). This grid is a global terrain elevation model at a 15 arc-second horizontal grid resolution. The grid was created by combining most recent SRTM15+ base grid with the gridded bathymetric datasets developed by the four Seabed 2030 Regional Centers. These gridded bathymetric data sets are primarily based on multibeam surveys where available. To get a smooth transition between these data sets GEBCO used a 'remove-restore' blending procedure based on satellite-derived bathymetry (Smith and Sandwell, 1997; Becker et al., 2009; Hell and Jakobsson, 2011). The GEBCO grid is advantageous because it combined direct measurements such as single beam, multibeam, and seismic measurements where available and indirect measurements, such as satellite-derived gravity data, and interpolates values based on an algorithm that weighs the quality of each data type. The final gridded dataset includes a type identifier that flags the source data that corresponds to each cell in the GEBCO grid. The data was downloaded from the GEBCO website (Gebco.net) within the region surrounding each individual transform fault.

2.2 Quantifying transform valley and ridge valley morphologic parameters

To characterize the morphology of each transform fault and the two adjacent ridge segments, I created transform and ridge perpendicular bathymetric profiles using the GEBCO bathymetry. To define the profiles, the GEBCO bathymetric grids were first imported into MATLAB, where I selected the two endpoints of each transform fault. These endpoints were chosen manually using the bathymetry to identify where the ridge valley and transform valley meet. These locations are typically bathymetric deeps corresponding to the intersection of the trace of the transform fault and ridge axis. Once the endpoints were selected, I defined a line connecting the two points and created ten equally spaced perpendicular topographic profiles along the transform fault (Figure 4). To minimize the impact of the asymmetry associated with the inside corner highs on the characterization of the transform valley, profiles were only taken across the middle 50% of the faults.

Figure 4: Bathymetry of the Oceanographer transform fault at 35ºN and the adjacent Mid-Atlantic Ridge spreading segments. The red circles show the endpoints selected for the end of the active transform fault and the ends of the adjacent ridge segments. 11 profiles were then measured in the central portion of the transform fault and the ridge segments adjacent to the transform fault.

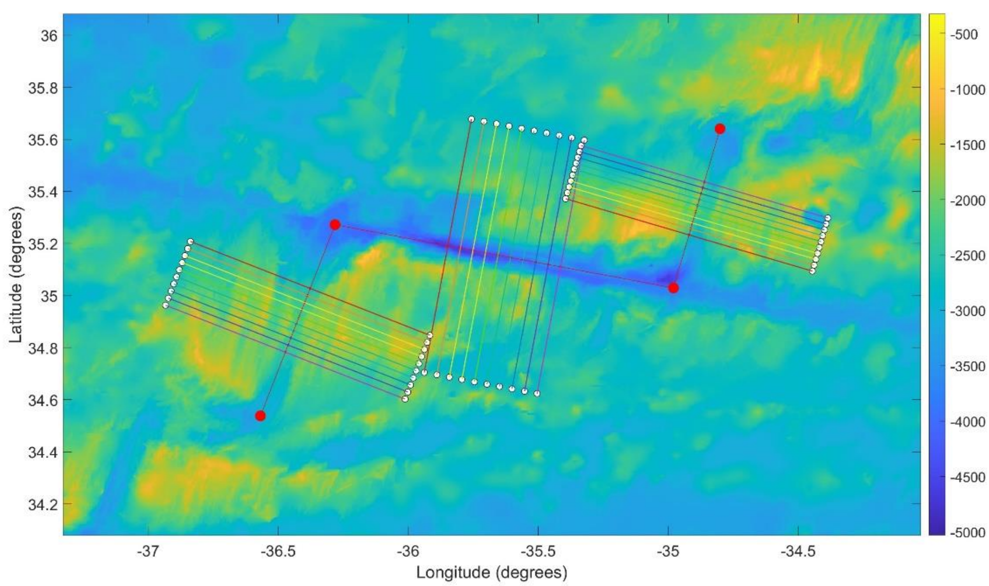

Similarly, for the two ridge segments bounding either side of the transform fault the corresponding endpoint is selected at the point where the segment ridge meets the next transform fault or non-transform offset (Figure 4). I again defined a line connecting the two ridge end points and created 10 equally spaced perpendicular topographic profiles along the central 50% of the ridge segment. In some cases, the adjacent spreading ridges and transform fault are not perfectly perpendicular to one another. When this occurs, the ridge-perpendicular profiles used to evaluate the morphology of the ridge valleys are not parallel to the transform fault. Analyzing profiles at the same locations, but forced to be parallel to the transform fault, I found that these small variations in the orientation of the ridge-perpendicular profiles did not significantly influence the inferred morphologic parameters of the ridge valleys.

Bathymetry was extracted from the GEBCO grid along each of the transform and ridge profiles to determine how the morphology of the transform and ridge valley varies along the length of the fault or ridge segment (Figure 5). The ten profiles were averaged to create a single mean profile for each transform fault and the adjacent ridge rift valleys (Figure 5). For each mean transform and ridge profile, the full width and half width, total relief, and depth of the transform and ridge valley were calculated (Figure 5). The valley half width was calculated based on the horizontal location of the midpoint in relief between the deepest point in the valley and the shallowest points on either side of the valley. Calculated in this way, the half width is often smaller than 50% of the full width. The total relief is defined as the average of the difference in elevation from the transform valley to the shallowest points on the two flanking highs. The same procedure was used to calculate the full width, half width, and total relief of the ridge valleys along the adjacent ridge segments.

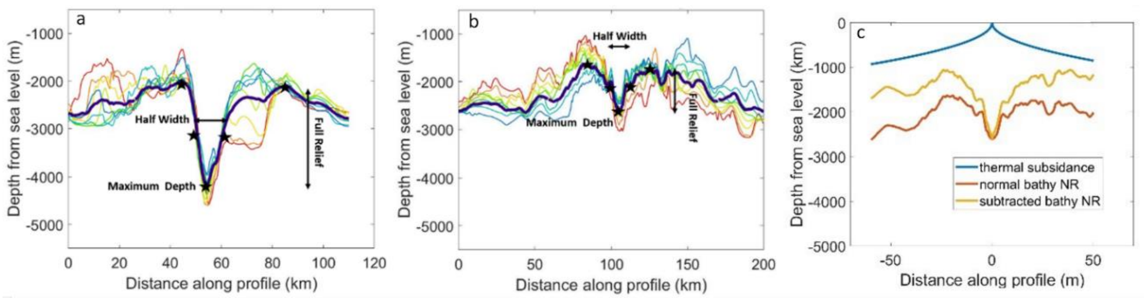

Figure 5: (a) Bathymetric profiles perpendicular to the Oceanographer transform fault, and (b) perpendicular to the spreading segment north of the transform. The colors of the profiles correspond to the profiles shown in Figure 4. The average profile is shown by the thick black line. The half width, full relief, and maximum depth are indicated for both the transform and ridge perpendicular profiles. (c) Calculated thermal subsidence as a function off-axis distance (blue) and the average bathymetry of the northern ridge valley before (red) and after (yellow) removing the thermal subsidence.

Assuming symmetric spreading at the adjacent ridge segments, the mean transform-perpendicular bathymetric profile should sample (on average) the same age lithosphere on both sides of the fault. By contrast, the bathymetry of the ridge-perpendicular profiles are affected by thermal subsidence with distance from the ridge axis. To evaluate the role of subsidence on the ridge axis parameters (ridge valley width and relief), the half-space cooling model was used to remove the thermal subsidence from the average ridge-perpendicular profile. I calculated the thermal subsidence, ω, with distance, x, from the ridge axis following Turcotte & Schubert (2014):

$$\omega = \frac{2\rho_m \alpha_v (T_1 - T_0)}{(\rho_m - \rho_w)} \left(\frac{\kappa x}{\pi u_0}\right)^{1/2} \quad , \tag{1}$$

here ρ_m and ρ_w are the density of the mantle and sea water, respectively; T_1 and T_o are the temperature of the mantle and the seafloor, respectively; $\alpha_v$is the coefficient of thermal expansion; κ is the thermal diffusivity of the mantle; and u_0 is the spreading rate. The choice of these parameters controls the rate at which the seafloor subsides as it cools and densifies as it moves away from the active ridge. These model predictions can be matched to seafloor bathymetry data. I assumed the density of the mantle and sea water to be 3370 kg/m^3 and 1026 kg/m^3, respectively; and the temperature of the mantle and seafloor to be 1350°C and 0°C, respectively. In addition, I set $\alpha_v = $ 3e-5 K^{-1} and κ = 10^{-6} m^2/s. The spreading rate was determined separately for each individual ridge segment based on the plate velocities. Figure 5c shows the average bathymetry of ridge segment to the north of the Oceanographer Transform Fault after thermal subsidence has been removed.

2.3 External geophysical and geological parameters

Lastly, I determined a series of external parameters for each transform fault, including fault length, fault slip rate, extension/compression rate across the transform, seismic coupling ratio, and the fault thermal area (Table 1). These external parameters were compared to the morphologic parameters to establish any relationships that can be used to infer the process by which transform valleys are created.

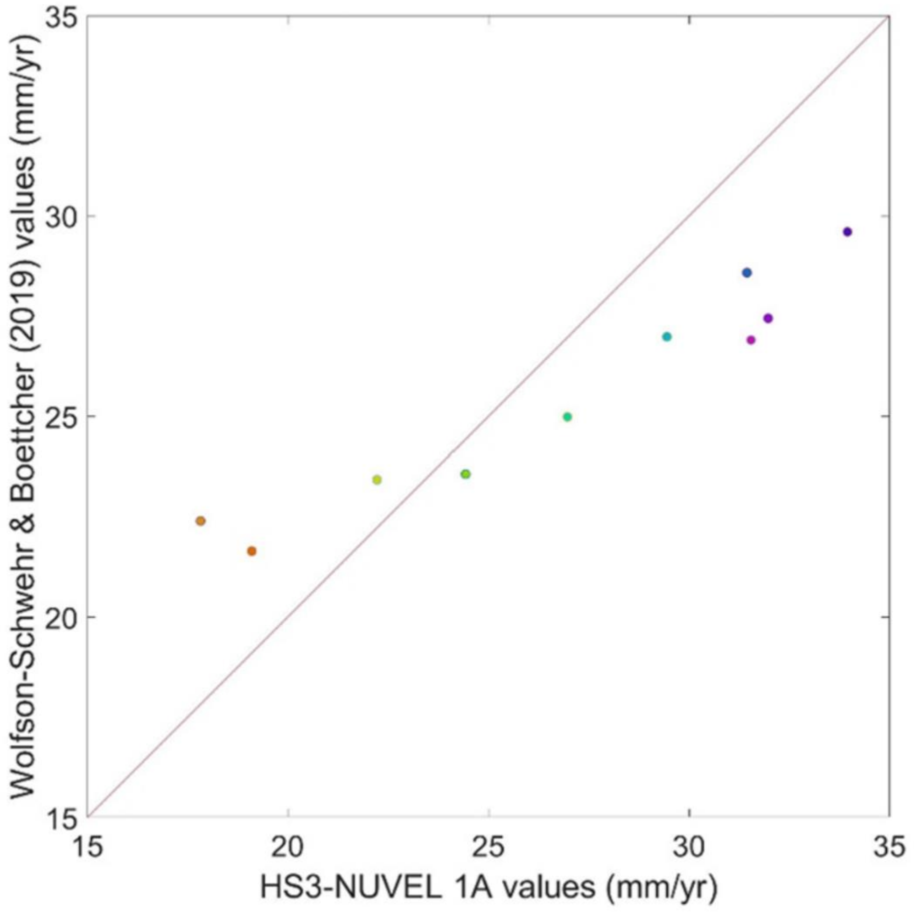

Figure 6: Comparison of the strike-slip fault-parallel velocities calculated for each transform fault versus those reported by Wolfson-Schwehr & Boettcher (2019).

Transform fault length was measured based on the end points chosen for each fault based on the GEBCO bathymetry data (e.g., Figure 4). To calculate fault slip rate and the rate of extension (or compression) across each fault, I used the UNAVCO plate motion calculator (https://www.unavco.org/software/geodetic-utilities/plate-motion-calculator/plate-motion-calculator.html). The calculator requires inputs of the latitude and longitude coordinates, plates IDs, and the plate motion model to determine the relative velocity between the two plates. For each fault, the coordinates were taken based on the northern-most point of the middle transform-perpendicular profile. I selected the plate south of each fault to be the reference plate and determined the relative velocity of the northern plate. I chose HS3-NUVEL 1A plate motion model (Gripp and Gordon, 2002), as this is the most recent hotspot reference frame model available in the UNAVCO plate motion calculator. Output from the UNAVCO plate motion calculator is given in terms of the north and east components of the plate velocity, and I converted these values into relative velocities parallel and perpendicular to the fault based on the strike of the transform as measured from the two endpoints selected for each fault. To benchmark my approach, I compared the fault-parallel slip values to those calculated by Wolfson-Schwehr & Boettcher (2019) for the same transform faults (Figure 6). I find the calculated velocities are consistent, with a slight offset and different slope, related to their use of an older plate-motion model, NUVEL-1.

The seismic coupling coefficient for each fault was taken from Wolfson-Schwehr & Boettcher (2019). The seismic coupling coefficient relates to the amount of fault slip accommodated by earthquakes to the total amount of slip based on the plate motion model. A coupling coefficient of 1 implies all slip is accommodated by earthquakes (i.e., co-seismic slip), while a coefficient of 0 means slip is fully aseismic.

Finally, the thermal area (A_T) was calculated using an equation from Boettcher and Jordan (2004) based on the length of the fault (L), the slip rate (V), and a constant (C_T) associated with the 600°C isotherm:

$$A_T = C_T L^{3/2} V^{-1/2} \tag{2}$$

The thermal area of the transform fault calculated in this way represents the brittle area of the lithosphere that is solid enough to experience fault slip as earthquakes.

These external parameters were chosen because they control different properties of the transform fault that may pertain to the formation of transform valleys. In the Discussion section, I compare these external parameters to the morphologic parameters calculated for each fault in order to quantitatively evaluate different models for transform valley formation.

3. Results

For each fault in this study, I compiled profiles of the bathymetry perpendicular to the center of the transform fault and to the centers of the adjacent ridge segments. Profiles for the Oceanographer transform fault at 35ºN along the Mid Atlantic Ridge and its adjacent ridges are shown in Figure 7. As described above, the transform-perpendicular profiles were taken over the central 50% of the transform fault to reduce the influence of the inside corner highs; however, some asymmetry can still be seen in the individual profiles (Figure 7C). The mean transform-perpendicular profile is more symmetrical than the individual profiles along the fault and is also smoother, reducing the effect of small-scale tectonic and volcanic features on the sea floor (Figures 7C–E).

Comparing the transform valley to the adjacent ridge valleys, I find that the Oceanographer transform valley is ~1720 m deeper than the ridge valleys (Figure 7F). However, after removing the effects of thermal subsidence (Figure 7G), the transform valley is only ~780 m deeper than the adjacent ridge valleys. The reason for this is that the center of ridge valley is situated on zero-age crust and thus its position does not shift in depth when corrected for thermal subsidence. By contrast, the mean transform valley profile is corrected upward to account for the appropriate amount of subsidence corresponding to the seafloor age at the center of the fault (Figure 7F-G). Correcting the mean transform profile does not influence its shape because the entire profile is on uniform age crust and hence the thermal correction does not change the width or relief of the transform valley. On the other hand, the thermal subsidence correction tends to widen the ridge valleys. This is caused by restoring the lithosphere to shallower depths off axis to account for mantle cooling as the plate moves away from the ridge axis. For example, adjacent to the Oceanographer transform fault, the mean ridge-perpendicular profile after thermal correction is 8.5 km wider to the north and 12.0 km wider to the south compared to the uncorrected bathymetry (Figure 7G). This process has been completed for each of the transform faults examined in this study and the individual results displayed similarly to Figure 7 are shown in the appendix.

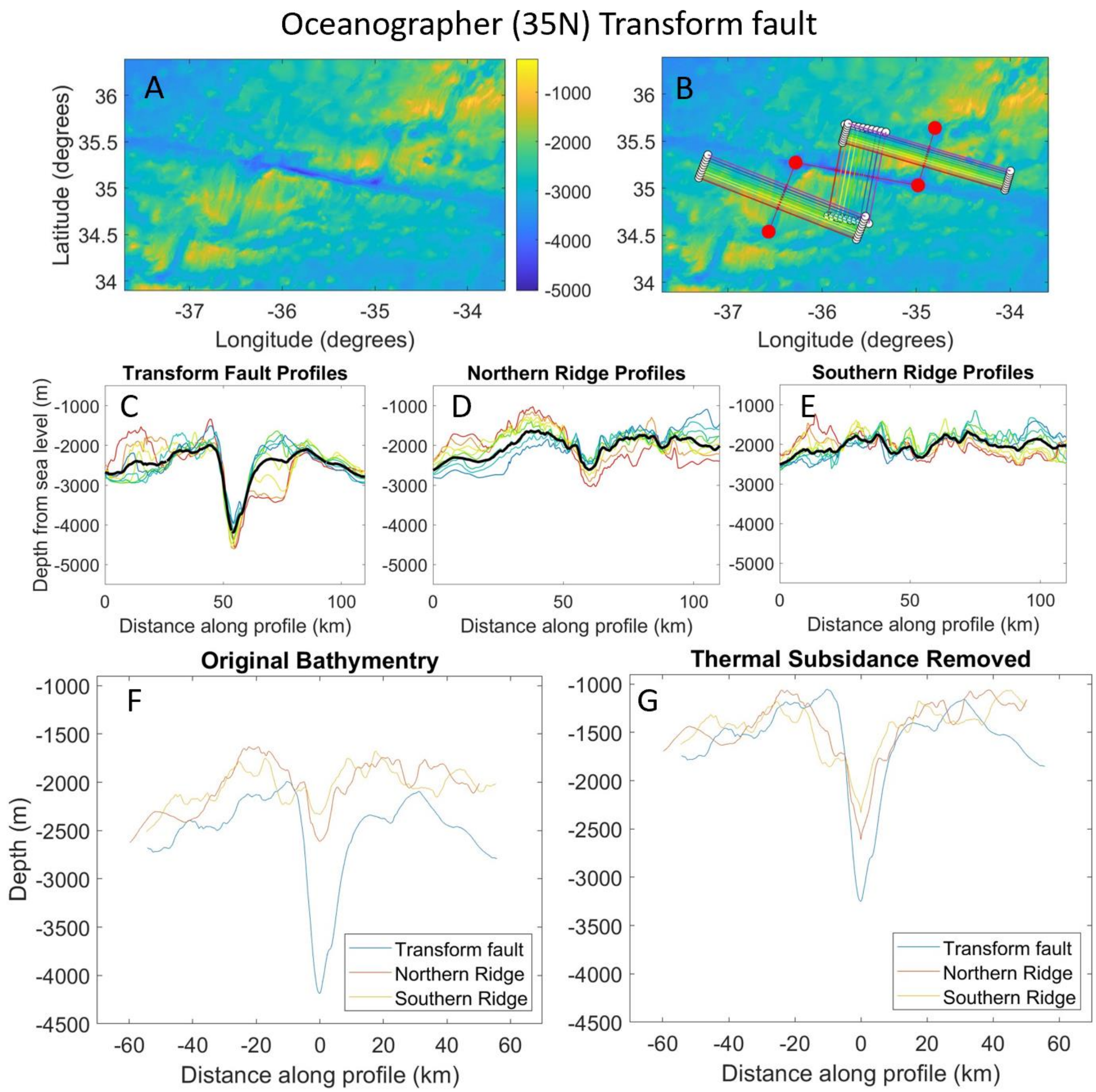

Figure 7: Oceanographer transform fault at 35ºN and adjacent ridges showing A) bathymetry and B) bathymetry with location of profiles identified. C–E) Bathymetry along individual profiles shown in (B) for the transform fault, northern ridge, and southern ridge, respectively. The average bathymetric profile is denoted with the thick black line. Panels (F) and (G) highlight how the average profiles compare before and after subtracting off the thermal subsidence of the tectonic plates, respectively.

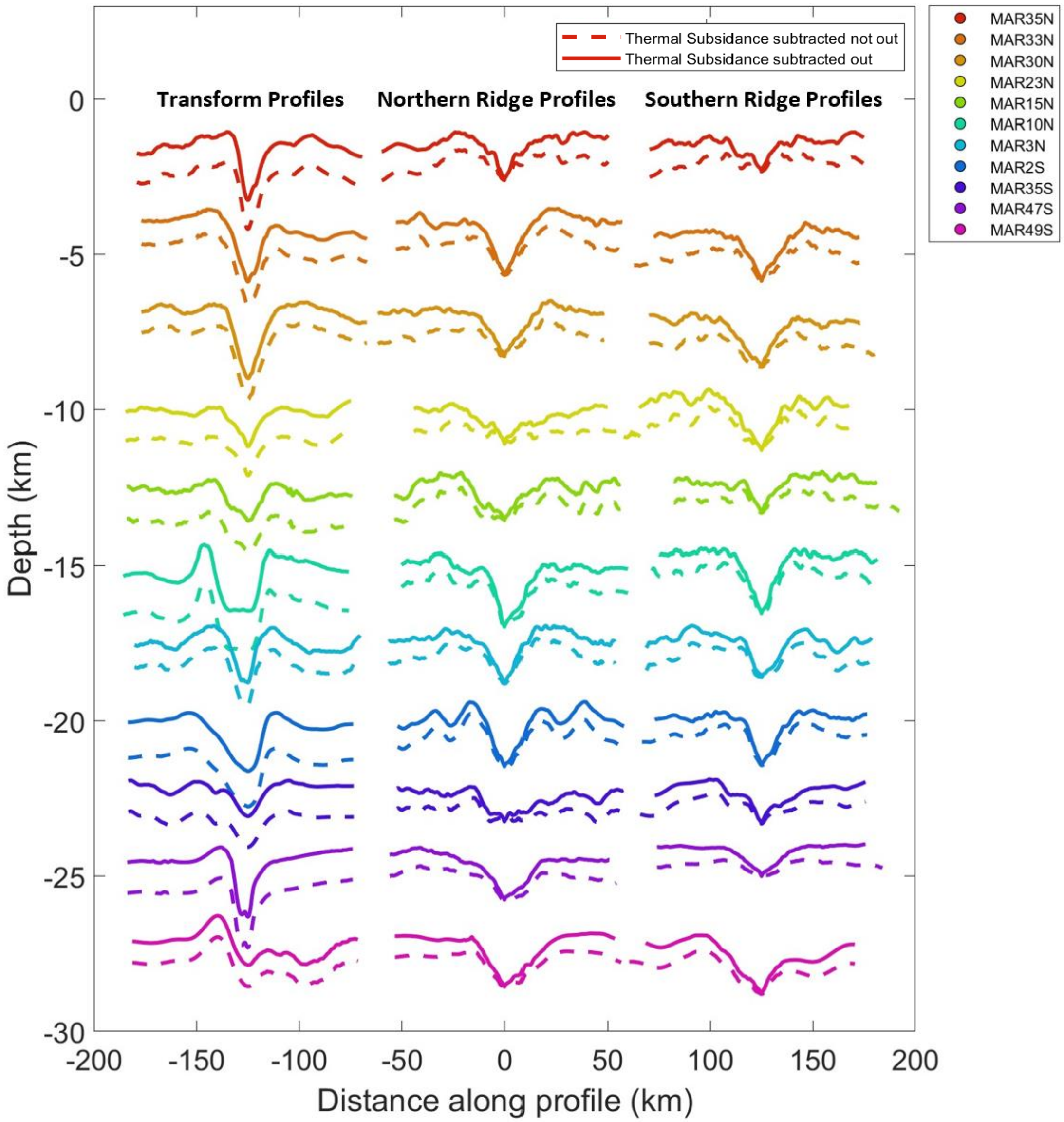

Figure 8: Mean bathymetric profile across the (left) transform fault, (middle) north ridge and (right) south ridge for each of the 11 transform systems investigated on the Mid-Atlantic Ridge. The dashed profiles show the original bathymetry, and the solid profiles show the thermally corrected profile after thermal subsidence is removed. Note that the transform faults are only shifted in depth relative to the original bathymetry because the age is the same on either side of transform. From top to bottom the faults are MAR 35ºN, MAR 33ºN, MAR 30ºN, MAR 23ºN, MAR 15ºN, MAR 10ºN, MAR 3ºN, MAR 2ºS, MAR 35ºS, MAR 47ºS, and MAR 49ºS. The colors of each fault correlate with the colors on the map in Figure 3.

To summarize the results from all the transform fault systems, we show the average transform profile, average northern ridge profile, and the average southern ridge profile for each fault before and after the thermal subsidence was subtracted from the profiles (Figure 8). Overall, removing the thermal subsidence resulted in shallower transform valleys and ridge valleys that become wider and but with greater total relief.

Morphological parameters were then computed from the thermally corrected bathymetry profiles and compared to one another to determine if any correlations exist between valley width, depth, and relief for the transform faults (Figure 9). Overall, transform valley relief increases with the maximum depth of the transform valley (R^2 = 0.36). Transform valley half width shows a weaker relationship, increasing only slightly with valley depth (R^2 = 0.17). Finally, no correlation was observed between valley half width and valley relief (R^2 =0.005).

Similarly, the morphological parameters for the adjacent ridge segments were compared to determine if any correlations exist between valley width, depth, and relief for either the northern or southern ridges (Figure 9). The northern ridges show the same primary trend between maximum depth and total relief as the transform faults (R^2 =0.24). The southern ridges have the strongest trend between the maximum depth and total relief (R^2 = 0.58. From these data it is apparent that the strongest correlation is between the relief and the depth for both the ridge and transform profiles, while in general there seems to be little to no correlation ($R^2 < 0.2$) between half width and relief and half width and depth for either the transform faults or the adjacent ridge segments.

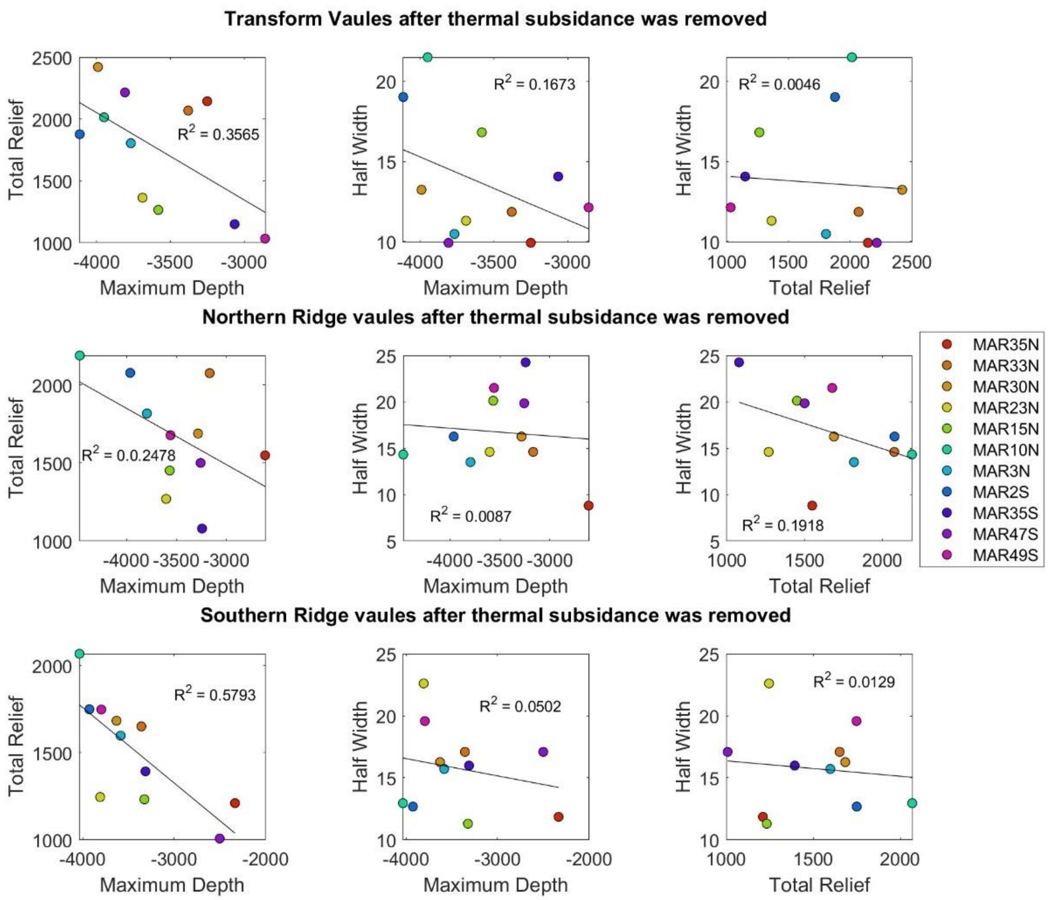

Figure 9: Comparison of the morphological parameters of the transform faults and corresponding ridges after the thermal subsidence was removed. Overall, the strongest correlation is found between total relief and maximum depth for both the transforms and the ridges. Weaker (or no) correlation is found between half width and maximum depth and half width and total relief.

Finally, I compared the morphologic parameters of the transform valleys with those of the adjacent ridge valleys before and after removing thermal subsidence (Figure 10). Before correcting for thermal subsidence, the transform valleys have similar widths compared to the adjacent ridge valleys (Figure 10A). The half widths of the ridges become even closer to the values of the transform faults after the thermal subsidence was removed (Figure 10B). Although most of the transform faults fall closely to the one-to-one line MAR 49°S has a much larger transform valley half width compared to the adjacent ridges. When comparing the total relief of the transform valleys to the uncorrected relief of the adjacent ridges, I find the transform valleys typically have larger relief than the ridge valleys (Figure 10C). However, after correcting for thermal subsidence, the total relief is more similar between the transform and ridge valleys (Figure 10D). Note that when correcting for thermal subsidence the relief does not change in the transform valleys because the entire profile is just shifted upward by a constant amount. The result is that the total relief is more similar after the correction because it adds to the ridge relief, but not to the transform valley relief.

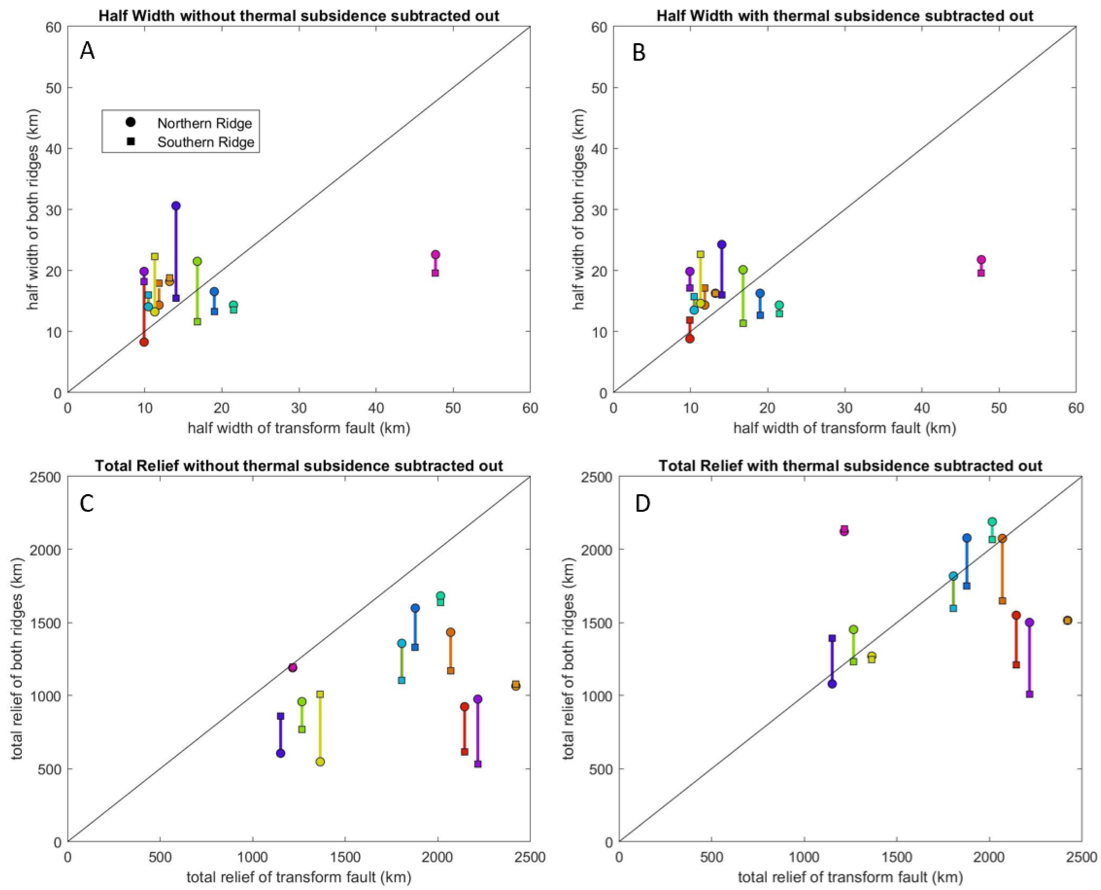

Figure 10: Comparison of the (A,B) total relief and (C,D) half width of the transform fault compared to the same parameters calculated for the adjacent ridges before and after correcting for thermal subsidence. Northern ridges are represented by filled squares, southern ridges with filled circles. Colors denote transform faults. Black solid lines denote 1-to-1 relationships.

4. Discussion

The results of this thesis indicate that oceanic spreading centers and oceanic transform faults on the slow-spreading Mid-Atlantic Ridge display similar morphologies. Both ridge axes and active transform faults are characterized by a deep valley flanked by uplifted ridges on either side. After removing the effect of thermal subsidence, the flanks of the ridges are corrected to shallower depth, resulting in total relief that is much closer to the relief across the transform valley (Figure 10 C-D). Further, the half widths of the ridge segments increase slightly after the thermal correction to become more similar to the half width of the adjacent transform fault; however, this effect is less pronounced primarily because the ridge and transform valley widths are already very similar (Figure 10 A-B).

Thus, taken together these results suggest very similar morphologies between active transform faults and their adjacent spreading centers. However, while the origin of rift valleys at slow spreading ridges is well understood from physical models of lithosphere undergoing extension (e.g., Buck et al, 2005), there remains no consensus on the origin of transform valley topography. Below I first summarize previous models for transform fault morphology and then discuss how they fit the observations along the Mid-Atlantic Ridge.

4.1 Models for transform fault morphology

Several models have been proposed to explain the formation of transform valleys. Transform faults form small circles around a Euler pole of rotation and depending on their offset direction will either have left- or right-lateral horizontal strike-slip motion. On a left-lateral transform fault, a counterclockwise change in spreading direction will cause compression in the active transform zone and extension for a clockwise change in plate motion. In the simplest case, trans-tension along a transform fault will promote normal faulting sub-parallel to the transform valley, similar to the fault-bounding normal faults observed on the flanks of mid-ocean ridge valleys. Pockalny et al. (1997) looked at the counterclockwise change in plate motion direction starting around 3 Ma at the fast-slipping Siqueiros transform fault. Because Siqueiros is a right-lateral fault, Pockalny et al. (1997) speculated that the counterclockwise change in plate motion promoted extension across the transform leading to the creation of the transform valley and intra-transform spreading centers. If this model is applicable to transform valleys globally, we would expect that transform valley morphology is directly comparable to mid-ocean ridge valley morphology and the valley walls might represent large normal faults (Pockalny et al., 1997). This model would also predict that any transform characterized by valley morphology must be experiencing trans-tension.

An alternative model is that the formation of a transform valley and adjacent transverse ridges on either side of the valley is caused by shear of a nonlinear viscoelastic rheology (Bercovici et al., 1992). In this model, the magnitude of transform fault topography is a function of the shear stress along the fault (Bercovici et al., 1992), which would in turn be related to the total brittle area of the fault combined with the mechanical coupling across the fault (Boettcher & Jordan, 2004). Here the brittle area is the portion of the fault that is cold enough to sustain high stresses and would be controlled by the fault thermal structure (e.g., Roland et al., 2010).

A final model predicts that transform valleys reflect the isostatic response of the seafloor to thinner crust at segment ends (Chen & Lin, 1999). Along-axis variations in crustal thickness are particularly pronounced at slow-spreading ridges where the three-dimensional pattern of mantle upwelling focus melt production to the center of spreading center (e.g., Lin et al., 1990; Lin and Phipps Morgan, 1993). In this model the transform valley width would reflect the along-axis gradient in crustal thickness.

4.2 Testing models for transform fault morphology with data

To test the models for transform valley morphology described above, I compared transform fault morphology to a series of external parameters including compression/extension rate across the transform, slip rate, fault length, fault thermal area, and seismic coupling coefficient (Table 1). Through this comparison, I hope to determine if the mechanisms controlling transform morphology are compatible with either an extensional mechanism or a model that involves the magnitude of shear stress along the fault.

Transform Fault	Latitude, Longitude endpoint 1	Latitude, Longitude endpoint 2	Slip rate (mm/yr)	Compression and extension values (mm/yr)	Length of fault (km)	Seismic Coupling Coefficient rate	Thermal Area (km^2)
MAR35N	(35.2, -36.2)	(35.0, -35.0)	18.8	0.42	121	0.420	1.26
MAR33N	(33.8, -39.1)	(33.6, -38.2)	19.1	-0.06	79.4	0.160	0.663
MAR30N	(30.1, -42.6)	(30.0, -42.0)	17.8	-2.61	58.5	0.060	0.434
MAR23N	(23.9, -46.3)	(23.6, -45.0)	22.2	0.78	142	0.210	1.47
MAR15N	(15.3, -46.7)	(15.2, -44.9)	24.4	3.25	191	0.040	2.19
MAR10N	(10.8, -43.7)	(10.7, -40.9)	27.0	0.42	310	0.480	4.31
MAR3N	(3.88, -32.6)	(3.95, -31.6)	29.4	4.18	109	0.020	0.85
MAR2S	(-1.54, -15.8)	(-0.88, -13.2)	31.4	14.0	303	0.330	3.85
MAR35S	(-35.5, -17.8)	(-35.2, -15.1)	34.0	11.1	246	0.500	2.71
MAR47S	(-47.6, -13.4)	(-47.0, -10.5)	32.0	15.6	230	0.040	2.53
MAR49S	(-49.3, -9.8)	(-49.0, -8.41)	31.5	16.2	109	0.010	0.832

Table 1: List of key fault parameters for each transform fault presented in this study.

The similarity observed topography in transform valley morphology and that of the adjacent ridge valleys, could potentially argue for a similar stretching process forming the topography in both settings. To test this idea, I compared the transform valley morphology to the rate of compression or extension across the transform fault (Figure 11, Table 2). For the data in this study to support a trans-tensional origin for transform valleys (Pockalny et.al, 1997), I would expect to see a correlation between valley relief and the extension rate across the transform fault. However, no clear correlation is found between the compression/extension rate and transform valley morphological parameters (Figure 11A-C). Specifically, the R^2 and P-values relating compression/extension rate and total relief (0.150, 0.239), valley half width (0.000440, 0.951), and maximum depth (0.0670, 0.465) dictate no correlation. Also, if the valley depth is controlled by extension, you would expect to see all the MAR transforms to be under next extension because all the transforms in this study had valleys. Instead, all but one of the transforms I investigated is under compression (Figure 11A-C). As this is contradictory to what the trans-tension model proposes, it is unlikely that extension is the main factor creating the transform valley.

Regression	**R^2**	**P-value**
Total Relief (km)		
Compression rate (mm/yr)	0.150	0.239
Slip rate (mm/yr)	0.215	0.151
Length of fault (km)	0.0119	0.750
Thermal area (km^2)	0.00109	0.923
Seismic Coupling Coefficient rate	0.000281	0.961
Half Width (km)		
Compression rate (mm/yr)	0.000440	0.951
Slip rate (mm/yr)	0.0377	0.567
Length of fault (km)	0.504	0.0144
Thermal area (km^2)	0.603	0.00494
Seismic Coupling Coefficient rate	0.189	0.181
Depth of Valley (km)		
Compression rate (mm/yr)	0.0670	0.465
Slip rate (mm/yr)	0.0143	0.726
Length of fault (km)	0.104	0.334
Thermal area (km^2)	0.149	0.242
Seismic Coupling Coefficient rate	0.00220	0.891

Table 2: List of R^2 and P-values for each of the panels in Figure 11. The significant values are highlighted with gray boxes.

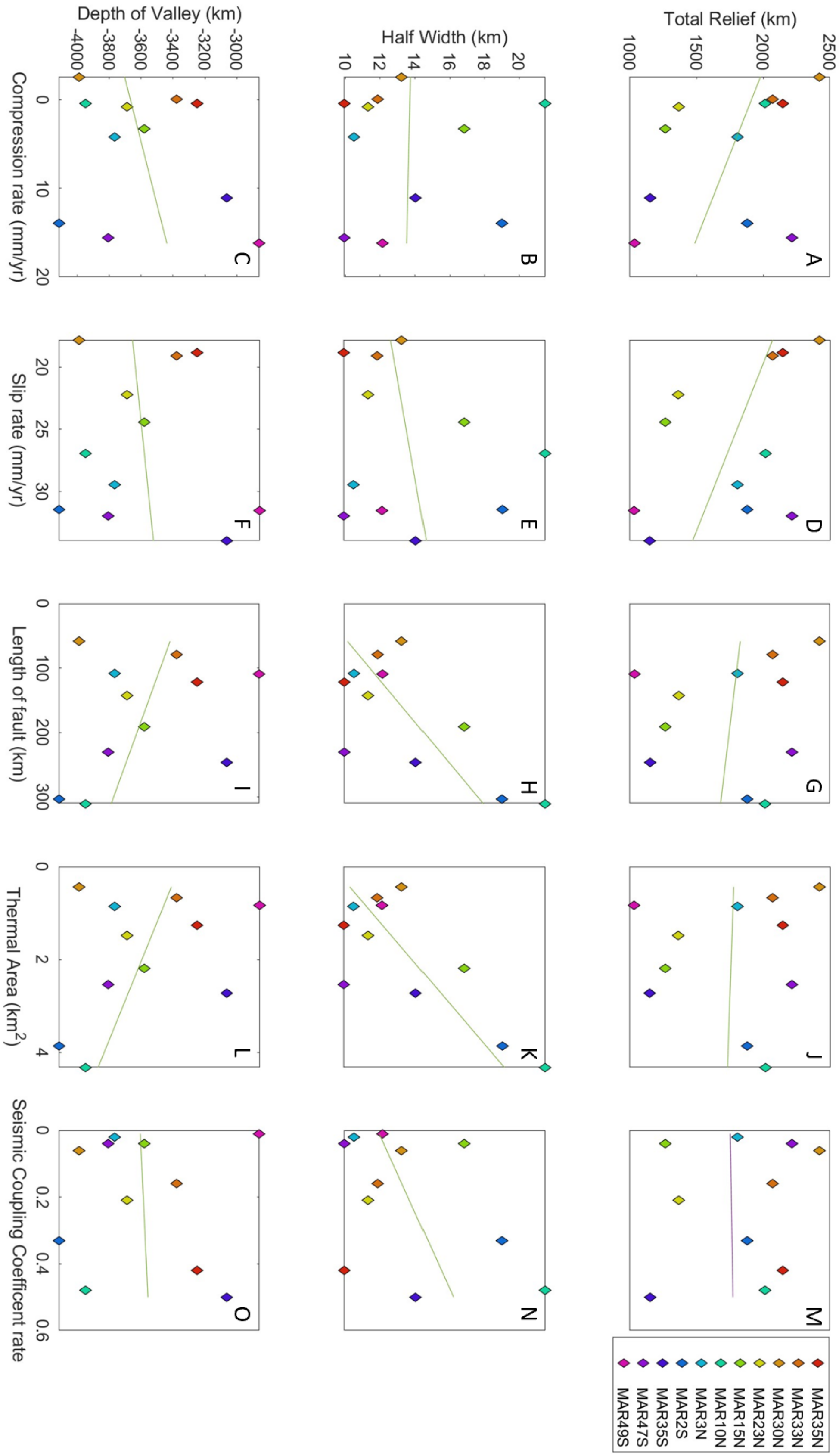

Total Relief (km)
Half Width (km)
Depth of Valley (km)
Compression rate (mm/yr)
Slip rate (mm/yr)
Length of fault (km)
Thermal Area (km^2)
Seismic Coupling Coefficent rate
A
B
C
D
E
F
G
H
I
J
K
L
M
N
O
MAR35N
MAR33N
MAR30N
MAR23N
MAR15N
MAR10N
MAR3N
MAR2S
MAR35S
MAR47S
MAR49S

Figure 11 (previous page): A comparison of the morphological parameters (total relief, half width and depth of the valley) with the external geophysical and geological parameters, such as the compression rate (A-C), the slip rate (D-F), the length of the fault (G-I), thermal area (J-L) and seismic coupling coefficient rate (M-O). In the left column, I use the convention that compression is shown with positive values and extension is shown with negative values. The R^2 and P-values for each figure are shown in Table 2.

I next investigated the idea that shear in a nonlinear viscoelastic rheology (e.g., Bercovici et al., 1992) could produce the observed transform valleys. If this model is correct, I would expect to see correlations between the morphological parameters and proxies for the shear stress on the fault. Assuming a fully coupled fault, the shear stress should increase with increasing fault thermal area (i.e., the area of the fault defined by the 600ºC isotherm) and the slip rate on the fault. Comparing the thermal area with transform valley morphology, I see the strongest correlation between thermal area and half width (R^2 = 0.603, P-value = 0.00494) (Figure 11K). However, transform valley relief (R^2 = 0.00109, P-value = 0.961) (Figure 11J) and depth (R^2 = 0.149, P-value = 0.242) (Figure 11L) have very weak correlations to fault thermal area. Finally, there is a weak negative correlation between slip rate and valley relief (R^2 = 0.215, P-value = 0.151) (Figure 11D); but this is the opposite trend that would be expected for increasing shear stress promoting deeper valleys. Thus, the nonlinear rheology model also cannot explain the full set of morphologic parameters.

In the calculation of stress above, I assumed that the 600ºC isotherm is a proxy for the maximum depth of earthquakes and thus the seismogenic area of the fault. However, it is also possible that some of the slip on the fault occurs by aseismic creep as opposed to earthquakes, and thus may not produce high shear stresses. To test this idea, I investigated the correlation between the morphologic parameters and the seismic coupling coefficient (Table 1). The seismic coupling coefficient is the ratio of the total seismic moment released in earthquakes divided by the theoretical seismic moment assuming all plate motion is accommodated by earthquakes (Boettcher & Jordan, 2004). A coupling coefficient of 0 would imply complete aseismic creep, while a coupling coefficient of 1 would imply all slip is accommodated by earthquakes. Here we might expect to see a positive correlation between seismic coupling coefficient (i.e., implying higher shear stresses) and morphology parameters. But again, while the strongest correlation is found between the seismic coupling coefficient and the half width (R^2 = 0.189, P-value = 0.181) (Figure 11N), there is very little correlation with either total relief (R^2 = 0.000281, P-value = 0.961) (Figure 11M) or maximum depth (R^2 = 0.00220, P-value =0.891) (Figure 11O).

Thus, overall, our data do not appear to be consistent with either a trans-tension or a nonlinear rheology model. This raises the question of whether isostatic compensation of crustal thickness variations as proposed by Chen & Lin (1999) could be a mechanism for the observed morphology at oceanic transform faults. Unfortunately, we do not currently have enough of the relevant data to test this model. Isostatic equilibrium is the gravitational balance such that the downward gravitational force of the topography (caused by the difference in density between water and crust) is equal to the upward buoyant force of the crustal roots (caused by the difference in density between crust and mantle). The result is that thicker crust should result in regions of elevated topography. Thinning of oceanic crust toward the ends of slow-spreading ridge segments is well established (Lin et al., 1990; Tolstoy et al., 1993; Detrick et al., 1995), and should result in deeper topography, consistent with the presence of transform valleys.

To test this model, you would need to constraint crustal thickness at the segment ends and along the transform. Future studies could use seismic and/or gravity data to estimate crustal thickness at each of the transform systems along the mid-Atlantic Ridge. The resultant crustal thickness estimates could then be compared to the transform valley morphologic parameters to see if the model successfully explains the data. Future studies could also test to see if the same relationships exist in transform faults on different ridge systems with different spreading rates. The morphology of fast-spreading ridges is very different than the slow spreading ridges on the Mid-Atlantic Ridge, yet more work is required to assess the variability in transform fault morphology across the full range of spreading rates. Insights from variations across spreading rates could yield additional information into the processes that are controlling transform valley formation.

5. Conclusion

In this thesis, I explored the morphology of oceanic transform faults on the slow spreading Mid-Atlantic ridge and compared their morphology to that of the adjacent mid-ocean ridge axes. To do this, I calculated three morphological parameters to describe each fault, namely the half width, total relief, and maximum depth. I find that the transform and ridge valleys are similar in their morphologic parameters when the effect of thermal subsidence is removed from the adjacent ridges. When comparing the morphological parameters found in this study to the external parameters characterizing each system, I find no evidence that transform valley morphology is controlled by trans-tension across the transform fault. I do find evidence that transform valley half width scales with shear stress, which can be an indication that transform valley morphology is at least in part controlled by the nonlinear viscoelastic response of the lithosphere to shear. However, the total relief and maximum depth of transform faults do not correlate with proxies for shear stress on the fault or far-field extension across the fault. Thus, it is possible these parameters are instead being controlled by isostatic compensation of crustal thickness variations.

Future studies should look deeper into the relationship between crustal thickness and transform fault morphology. Future studies could also determine if these same trends that were found on slow spreading ridge transform faults exist in transform faults on mid-ocean ridges of varying spreading rates.

Appendix

The following figures show the bathymetry, the location of profiles, the profiles and average profile of the transform fault and each adjacent ridge, and how these average profiles compare before and after subtracting off the thermal subsidence of the tectonic plates. These figures are replicas of Figure 7 in the results section for each transform fault presented in this study.

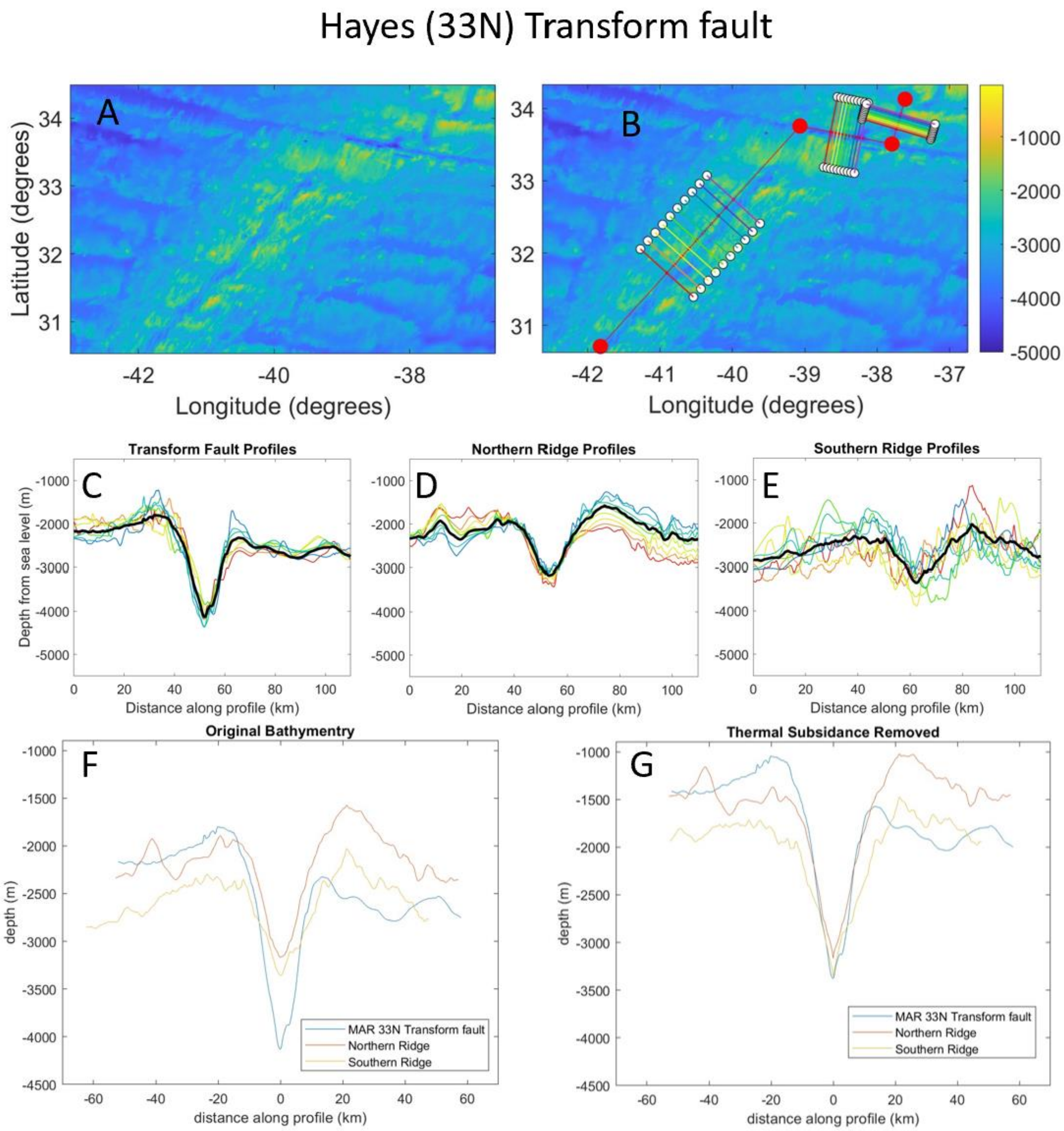

Figure A1-1: database figures of Transform fault MAR 33N showing bathymetry, the location of profiles, the profiles and average profile of the transform fault and each adjacent ridge, and how these average profiles compare before and after subtracting off the thermal subsidence of the tectonic plates.

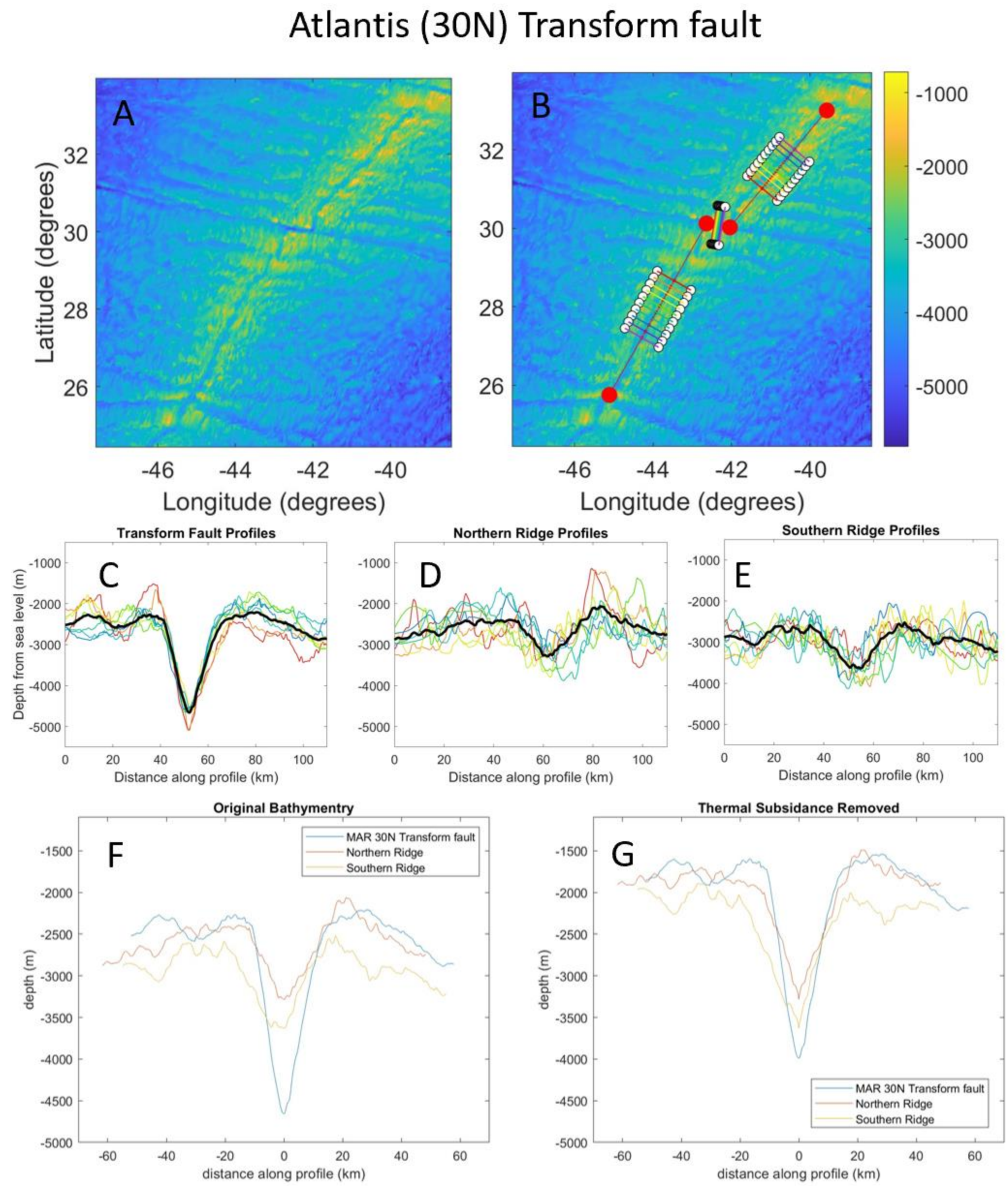

Figure A1-2: database figures of Transform fault MAR 30N showing bathymetry, the location of profiles, the profiles and average profile of the transform fault and each adjacent ridge, and how these average profiles compare before and after subtracting off the thermal subsidence of the tectonic plates.

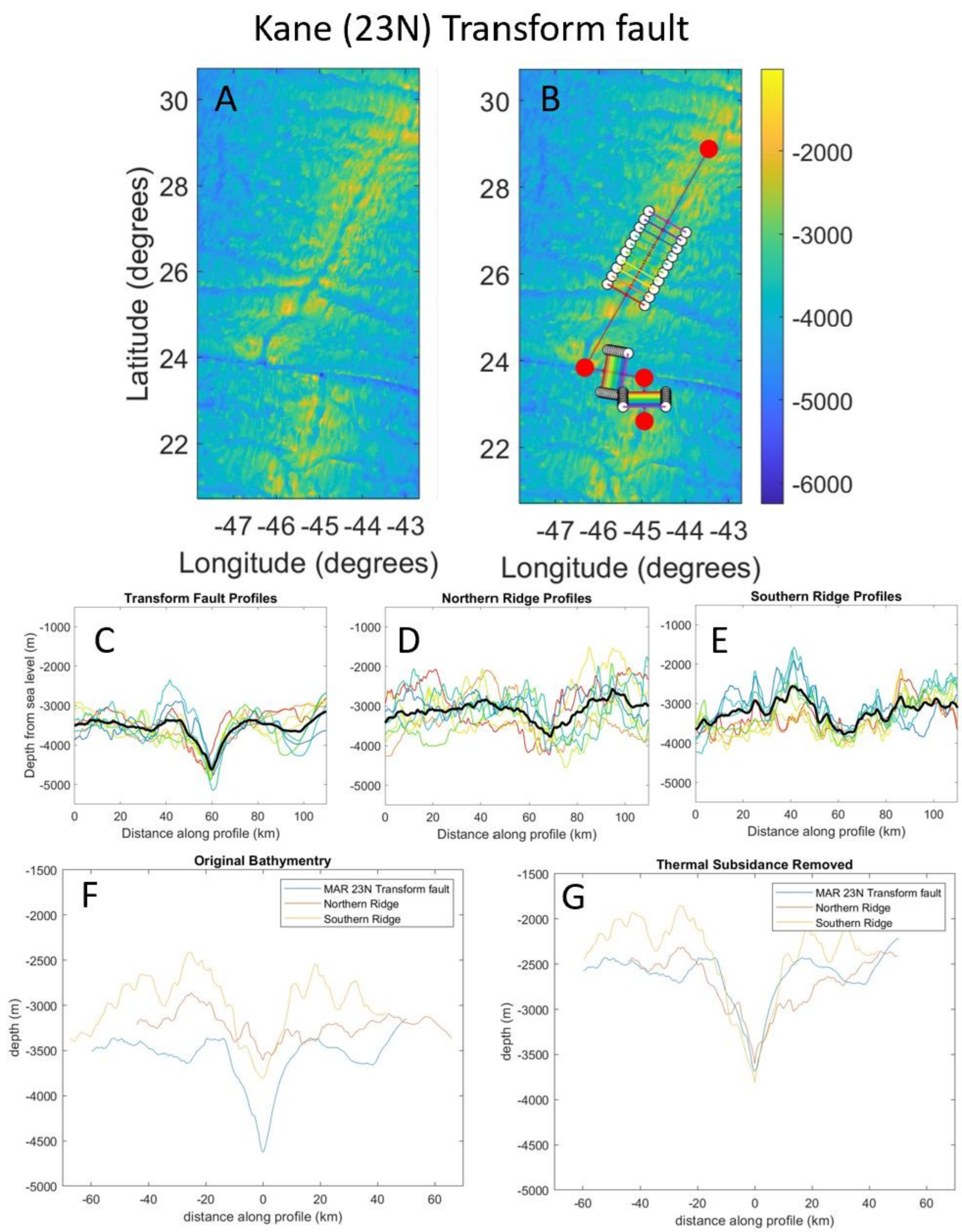

Figure A1-3: database figures of Transform fault MAR 23N showing bathymetry, the location of profiles, the profiles and average profile of the transform fault and each adjacent ridge, and how these average profiles compare before and after subtracting off the thermal subsidence of the tectonic plates.

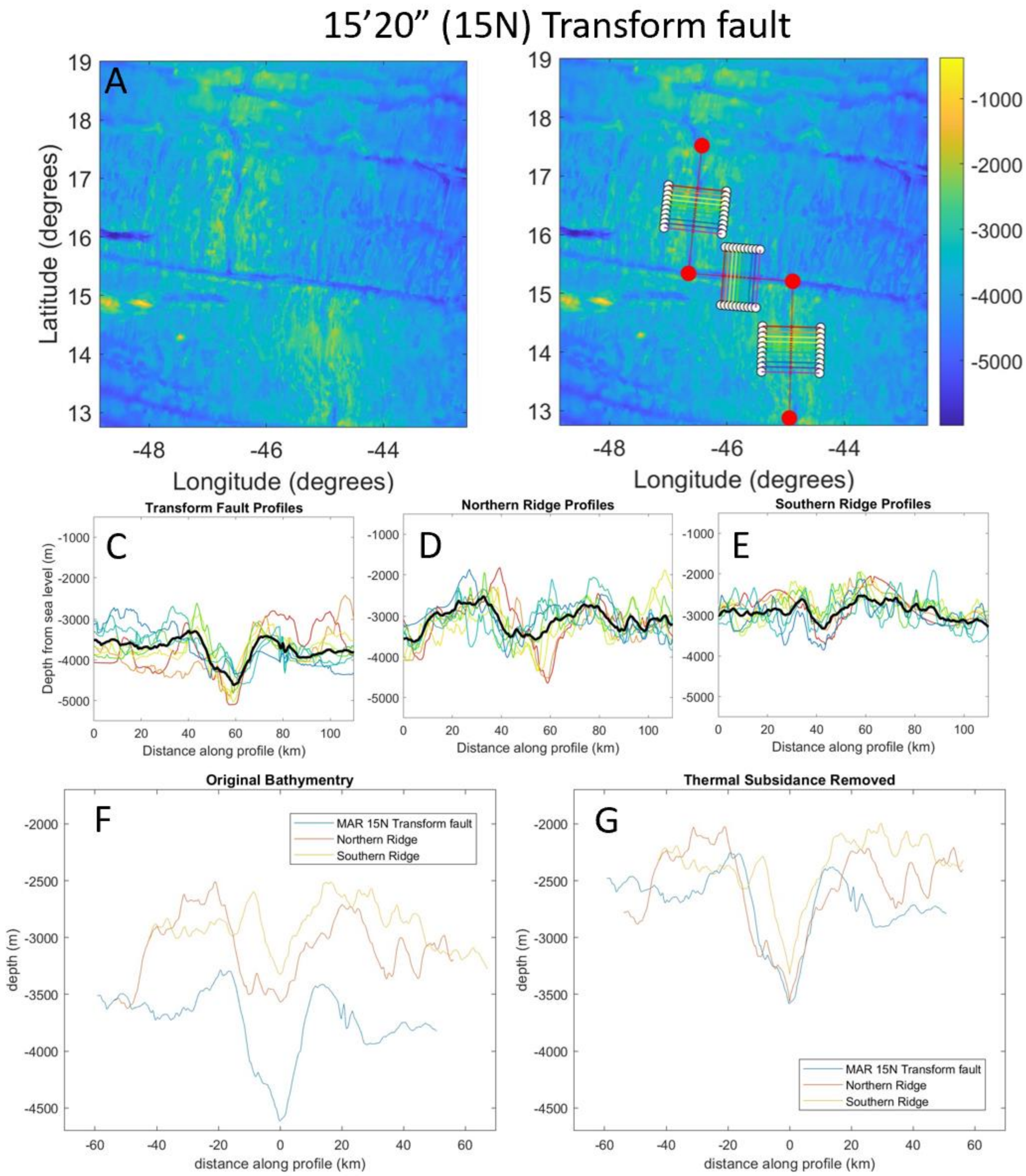

Figure A1-4: database figures of Transform fault MAR 15N showing bathymetry, the location of profiles, the profiles and average profile of the transform fault and each adjacent ridge, and how these average profiles compare before and after subtracting off the thermal subsidence of the tectonic plates.

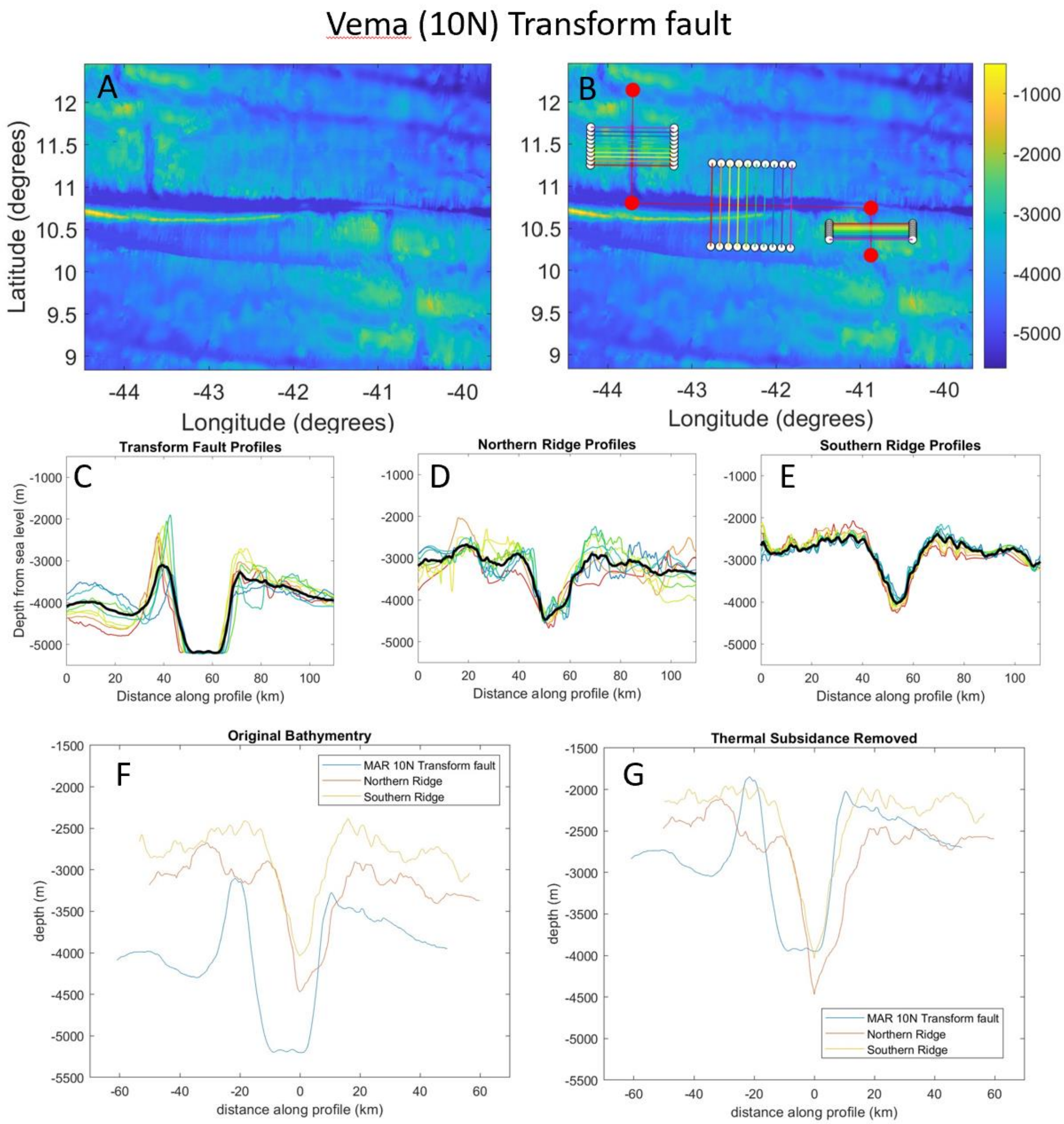

Figure A1-5: database figures of Transform fault MAR 10N showing bathymetry, the location of profiles, the profiles and average profile of the transform fault and each adjacent ridge, and how these average profiles compare before and after subtracting off the thermal subsidence of the tectonic plates.

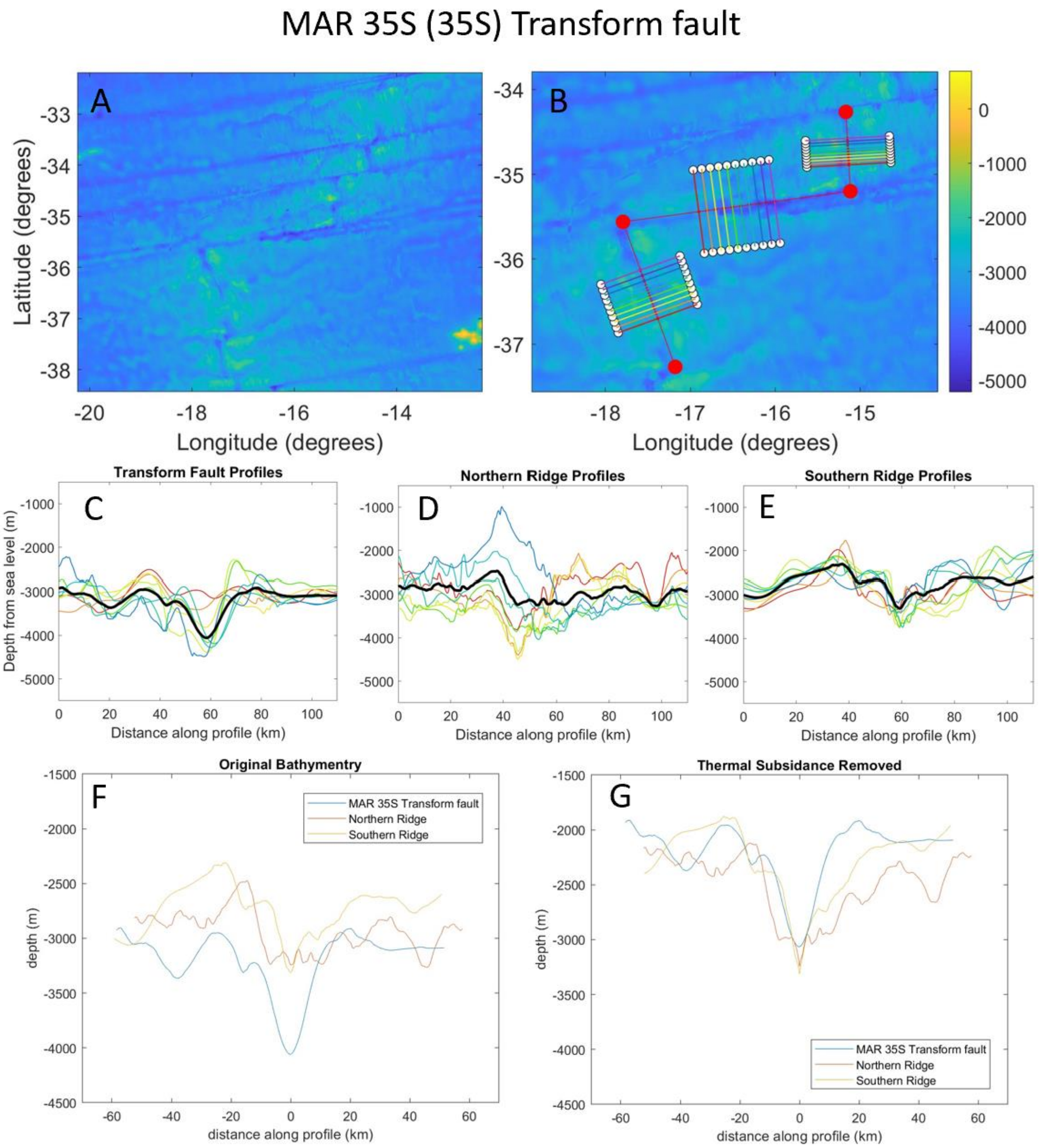

Figure A1-6: database figures of Transform fault MAR 35S showing bathymetry, the location of profiles, the profiles and average profile of the transform fault and each adjacent ridge, and how these average profiles compare before and after subtracting off the thermal subsidence of the tectonic plates.

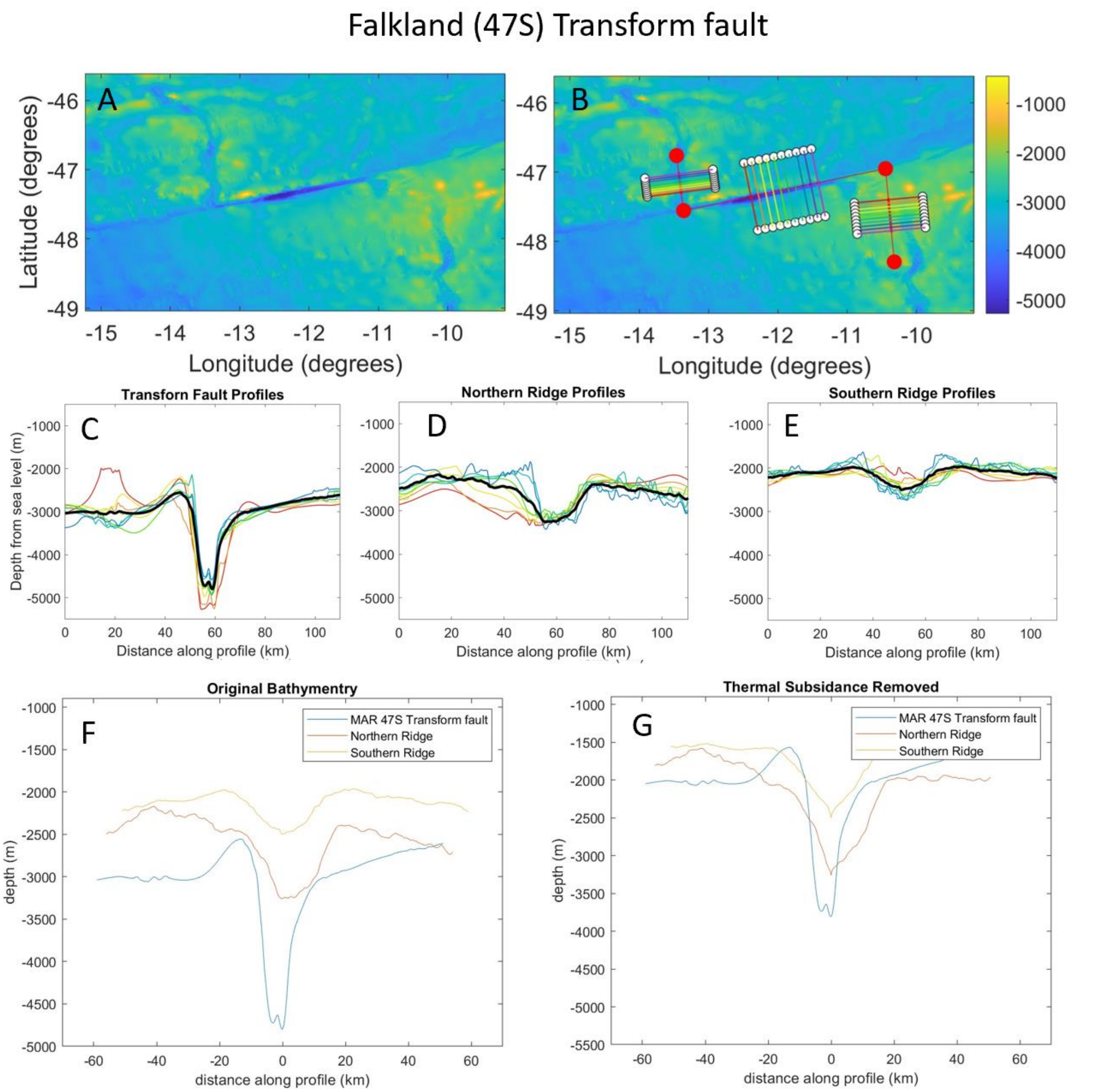

Figure A1-7: database figures of Transform fault MAR 47S showing bathymetry, the location of profiles, the profiles and average profile of the transform fault and each adjacent ridge, and how these average profiles compare before and after subtracting off the thermal subsidence of the tectonic plates.

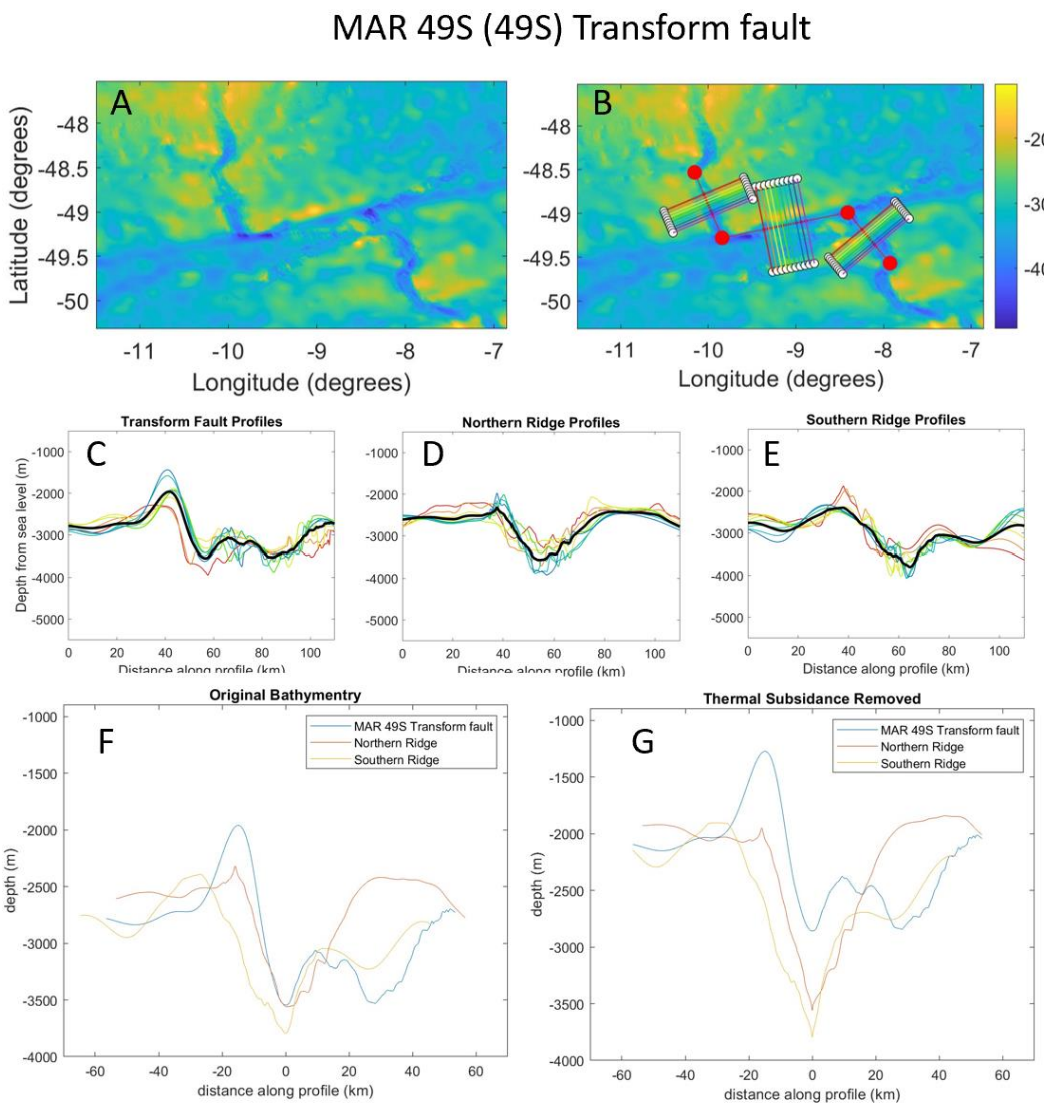

Figure A1-8: database figures of Transform fault MAR 49S showing bathymetry, the location of profiles, the profiles and average profile of the transform fault and each adjacent ridge, and how these average profiles compare before and after subtracting off the thermal subsidence of the tectonic plates.

References

Behn, M. D. & Ito, G. Magmatic and tectonic extension at mid-ocean ridges: 1. Controls on fault characteristics. Geochem Geophys Geosystems 9, Q08O10-n/a (2008).

Bercovici, David, et al. “Nonlinear Viscoelasticity and the Formation of Transverse Ridges.” *Journal of Geophysical Research*, vol. 97, no. B10, 1992, p. 14195. *DOI.org (Crossref)*, doi:10.1029/92JB00890.

Boettcher, M. S. & Jordan, T. “Earthquake Scaling Relations for Mid-Ocean Ridge Transform Faults.” *Journal of Geophysical Research*, vol. 109, no. B12, 2004, p. B12302. *DOI.org (Crossref)*, doi:10.1029/2004JB003110.

Buck, W. Roger, et al. “Modes of Faulting at Mid-Ocean Ridges.” *Nature*, vol. 434, no. 7034, Apr. 2005, pp. 719–23. *DOI.org (Crossref)*, https://doi.org/10.1038/nature03358.

Cann, J. R., et al. “Corrugated Slip Surfaces Formed at Ridge–Transform Intersections on the Mid-Atlantic Ridge.” *Nature*, vol. 385, no. 6614, Jan. 1997, pp. 329–32. *DOI.org (Crossref)*, https://doi.org/10.1038/385329a0.

Chen, Y. & Lin, J. Mechanisms for the formation of ridge-axis topography at slow-spreading ridges: a lithospheric-plate flexure model. Geophys. J. Int. 136, 8–18 (1999).

Choblet, G. And Parmentier, E. M. Mantle upwelling and melting beneath slow spreading centers: effects of variable rheology and melt productivity. Earth Planet Sci. Lett., 184, 589–604 (2001).

Craig, T. J., Copley, A. & Jackson, J. A reassessment of outer-rise seismicity and its implications for the mechanics of oceanic lithosphere. *Geophys J Int* 197, 63–89 (2014).

Detrick, R. S., Needham, H. D. & Renard, V. Gravity anomalies and crustal thickness variations along the Mid-Atlantic Ridge between 33°N and 40°N. J Geophys Res Solid Earth 100, 3767–3787 (1995).

GEBCO Compilation Group (2021) GEBCO 2021 Grid (doi:10.5285/c6612cbe-50b3-0cff-e053-6c86abc09f8f)

Grevemeyer, Ingo, et al. “Extensional Tectonics and Two-Stage Crustal Accretion at Oceanic Transform Faults.” *Nature*, vol. 591, no. 7850, Mar. 2021, pp. 402–07. *DOI.org (Crossref)*, doi:10.1038/s41586-021-03278-9.

Heezen, B.C. (1960) The Rift in the Ocean Floor. Scientific American, 203, 98-110. http://dx.doi.org/10.1038/scientificamerican1060-98

Karson, J. A. *et al.* The geology of the Oceanographer Transform: The ridge-transform intersection. *Mar Geophys Res* 6, 109–141 (1984).

Karson, J. A., and H. J. B. Dick. “Tectonics of Ridge-Transform Intersections at the Kane Fracture Zone.” *Marine Geophysical Researches*, vol. 6, no. 1, 1983, pp. 51–98. *DOI.org (Crossref)*, https://doi.org/10.1007/BF00300398.

Kelemen, Peter B. “The Origin of the Land under the Sea.” *Scientific American*, vol. 300, no. 2, Feb. 2009, pp. 52–57. *DOI.org (Crossref)*, doi:10.1038/scientificamerican0209-52.

Lin, John, et al. “Evidence from Gravity Data for Focused magmatic Accretion along the Mid-Atlantic Ridge.” Nature, vol. 344, no. 6267, Apr. 1990, pp. 627–32. DOI.org (Crossref), https://doi.org/10.1038/344627a0.

Lin, J. & Parmentier, E. Mechanics of lithospheric extension at mid-ocean ridges. *Geophys. Jour.* 96, 1–22 (1989).

Lin, J., Purdy, G., Schouten, H., Sempéré, J.-C. & Zervas, C. Evidence from gravity data for focused magmatic accretion along the Mid-Atlantic ridge. Nature 344, 627–632 (1990).

Luo, Y., Lin, J., Zhang, F., & Wei, M. (2021). Spreading rate dependence of morphological characteristics in global oceanic transform faults. Acta Oceanologica Sinica, 40(4), 39–64. https://doi.org/10.1007/s13131-021-1722-5

Macdonald, K. C. Mid-Ocean Ridges: Fine Scale Tectonic, Volcanic and Hydrothermal Processes Within the Plate Boundary Zone. *Annual Review of Earth and Planetary Sciences* 10, 155–190 (1982).

Macdonald, K. C., Fox, P. J., Perram, L. J. & Eisen, M. F. A new view of the mid-ocean ridge from the behaviour of ridge-axis discontinuities. *Nature* (1988).

Morgan, Jason Phipps, and Y. John Chen. “The Genesis of Oceanic Crust: Magma Injection, Hydrothermal Circulation, and Crustal Flow.” *Journal of Geophysical Research: Solid Earth*, vol. 98, no. B4, Apr. 1993, pp. 6283–97. *DOI.org (Crossref)*, https://doi.org/10.1029/92JB02650.

Morrow, Thomas A., et al. “Are Segmented Fracture Zones Weak? Analytical and Numerical Models Constrain Anomalous Bathymetry at the Clarion and Murray Fracture Zones.” *Earth and Planetary Science Letters*, vol. 512, Apr. 2019, pp. 214–26. *DOI.org (Crossref)*, https://doi.org/10.1016/j.epsl.2019.02.010.

Neumann, G. A. & Forsyth, D. W. The paradox of the axial profile: Isostatic compensation along the axis of the Mid-Atlantic Ridge? J Geophys Res Solid Earth 98, 17-891-17–910 (1993).

Parmentier, E. M., and Jason Phipps Morgan. “Spreading Rate Dependence of Three-Dimensional Structure in Oceanic Spreading Centres.” *Nature*, vol. 348, no. 6299, Nov. 1990, pp. 325–28. *DOI.org (Crossref)*, https://doi.org/10.1038/348325a0.

Parsons, Barry, and John G. Sclater. “An Analysis of the Variation of Ocean Floor Bathymetry and Heat Flow with Age.” *Journal of Geophysical Research*, vol. 82, no. 5, Feb. 1977, pp. 803–27. *DOI.org (Crossref)*, https://doi.org/10.1029/JB082i005p00803.

Pockalny, R. A., Gente, P. & Buck, R. Oceanic transverse ridges: A flexural response to fracture-zone–normal extension. *Geology* 24, 71–74 (1996).

Reston, T. J., et al. “A Rifted inside Corner Massif on the Mid-Atlantic Ridge at 5°S.” Earth and Planetary Science Letters, vol. 200, no. 3–4, pp. 255–69, 2002

Roland, Emily, et al. “Seismic Velocity Constraints on the Material Properties That Control Earthquake Behavior at the Quebrada-Discovery-Gofar Transform Faults, East Pacific Rise: SEISMIC CONSTRAINTS AT EPR TRANSFORMS.” *Journal of Geophysical Research: Solid Earth*, vol. 117, no. B11, Nov. 2012, p. n/a-n/a. *DOI.org (Crossref)*, https://doi.org/10.1029/2012JB009422.

Schierjott, J.C., G. Apuzen-Ito, M.D. Behn, X. Tian, T. Morrow, B.J.P. Kaus, and J. Escartín, 2023, How transform fault shear influences where detachment faults form near mid-ocean ridges, Scientific Reports, v. 13, 9259, https://doi.org/10.1038/s41598-023-35714-3.

Schouten, Hans, et al. “Segmentation of Mid-Ocean Ridges.” *Nature*, vol. 317, no. 6034, Sept. 1985, pp. 225–29. *DOI.org (Crossref)*, https://doi.org/10.1038/317225a0.

Sempéré, J.-C., Lin, J., Brown, H. S., Schouten, H. & Purdy, G. M. Segmentation and morphotectonic variations along a slow-spreading center: The Mid-Atlantic Ridge (24o00’N-30o40’N). *Mar Geophys Res* 15, 153–200 (1993).

Searle, Roger. *Mid-Ocean Ridges*. Cambridge University Press, 2013.

Shaw, W. J. & Lin, J. Models of ocean ridge lithospheric deformation: Dependence on crustal thickness, spreading rate, and segmentation. *J Geophys Res Solid Earth* 101, 17977–17,993 (1996).

Sleep, Norman H., and Shawn Biehler. “Topography and Tectonics at the Intersections of Fracture Zones with Central Rifts.” *Journal of Geophysical Research*, vol. 75, no. 14, May 1970, pp. 2748–52. *DOI.org (Crossref)*, https://doi.org/10.1029/JB075i014p02748.

Stein, C. A. & Stein, S. A model for the global variation in oceanic depth and heat flow with lithospheric age. Nature 359, 123–129 (1992).

Sykes, L.R., 1967. Mechanisms of earthquakes and nature of faulting on mid-ocean ridges. J.Geophy. Res. 72, 2131-2153

Talwani, Manik, et al. "Reykjanes Ridge Crest: A Detailed Geophysical Study." *Journal of Geophysical Research*, vol. 76, no. 2, Jan. 1971, pp. 473–517. *DOI.org (Crossref)*, https://doi.org/10.1029/JB076i002p00473.

Tucholke, Brian E., and Hans Schouten. "Kane Fracture Zone." *Marine Geophysical Researches*, vol. 10, no. 1–2, Mar. 1988, pp. 1–39. *DOI.org (Crossref)*, https://doi.org/10.1007/BF02424659.

Tolstoy, M., Harding, A. & Orcutt, J. Crustal thickness on the Mid-Atlantic Ridge: Bull's-eye gravity anomalies and focused accretion. Science 262, 726–729 (1993).

Watts, A. B., Bodine, J. H., & Steckler, M. S. (1980). Observations of flexure and the state of stress in the oceanic lithosphere. *Journal of Geophysical Research: Solid Earth*, *85*(B11), 6369–6376. https://doi.org/10.1029/jb085ib11p06369

Wilson, J. T., A new class of faults and their bearing on continental drift, Nature, 207, 343-347, 1965

Wolfson-Schwehr, M., & Boettcher, M. S. (2019). Global characteristics of oceanic transform fault structure and seismicity. *Transform Plate Boundaries and Fracture Zones*, 21–59. https://doi.org/10.1016/b978-0-12-812064-4.00002-5